

# Dilepton production in proton-nucleus and nucleus-nucleus collisions at SPS energies

G. Q. Li and C. M. Ko

*Cyclotron Institute and Physics Department, Texas A&M University,*

*College Station, TX 77843, USA*

G. E. Brown and H. Sorge

*Department of Physics, State University of New York at Stony Brook, Stony Brook, NY 11974,*

*USA*

## Abstract

Dilepton production in proton- and nucleus-induced reactions is studied in relativistic transport model using initial conditions determined by the string dynamics from RQMD. It is found that both the CERES and HELIOS-3 data for dilepton spectra in proton-nucleus reactions can be well described by the ‘conventional’ mechanism of Dalitz decay and direct vector meson decay. However, to provide a quantitative explanation of the observed dilepton spectra in central S+Au and S+W collisions requires contributions other than these direct decays. Introducing a decrease of vector meson masses in hot and dense medium, we find that these heavy-ion data can also be satisfactorily explained. This agrees with our earlier conclusions based on a fire cylinder model. We also give predictions for Pb+Au collisions at 160 GeV/nucleon using current CERES mass resolution and acceptance.

Typeset using REVTeX

## I. INTRODUCTION

In future experiments at the relativistic heavy-ion collider (RHIC) [1], dilepton production will play an important role in the search for signals of the quark-gluon plasma. Since dileptons interact only electromagnetically with the hadronic environment, they are thus penetrating probes of the early, most violent stage of heavy-ion collisions, where one expects that the quark-gluon plasma is likely to be created [2–12]. However, dileptons are produced in all stages of ultra-relativistic heavy-ion collisions. In the initial stage, Drell-Yan processes are important and contribute essentially to dileptons with large invariant mass [13]. They are also produced from hadronic interactions as well as hadronic decays. These dileptons have most likely low to intermediate invariant masses. Thus, in order to deduce useful information about the quark-gluon plasma from dilepton spectra, it is important to have a good and accurate understanding of dilepton production from both initial Drell-Yan processes and later stage hadronic interactions.

Furthermore, the study of dilepton production from hadronic interactions carries useful information about hadron properties in hot and dense hadronic matter, which are expected to be different from those in free space due to the partial restoration of chiral symmetry. There have already been suggestions to use dileptons to study the medium modification of pion dispersion relation at both finite density and temperature [14,15], the hadron electromagnetic form factor in dense matter [16], and in-medium properties of vector mesons [17–22].

A particular useful aspect of dileptons is that their spectrum produced from the hadronic matter may reflect directly the in-medium vector meson masses, which have been shown in certain models to decrease with increasing density and/or temperature [23–30]. Dileptons have already been measured at Bevalac by the DLS collaboration [31] in heavy-ion collisions at incident energies around 1 GeV/nucleon. Theoretical studies have shown that the observed dileptons with invariant mass above about 450 MeV are mainly from pion-pion annihilation [16,32]. Since the pion electromagnetic form factor is dominated by the rho meson, measuring dileptons from heavy-ion collisions thus provides the possibility of study-

ing the properties of rho meson in hot and dense matter. Unfortunately, statistics are not good enough in the Bevalac experiments to give definite information on the in-medium rho meson properties. However, similar experiments with vastly improved statistics have been planned at SIS by the HADES collaboration [33].

On the other hand, recent observation of the enhancement of low-mass dileptons in central S+Au and S+W collisions at SPS/CERN energies by the CERES [34] and the HELIOS-3 [35] collaboration, respectively, has generated a great deal of interest in heavy-ion community. Different dynamical models, such as hydrodynamical and transport models, have been used to investigate this phenomenon [36–39]. Although several different mechanisms [36–43] have been put forward to explain the observed enhancement, the most consistent explanation seems to be the decrease of vector meson masses in hot and dense matter [36–38]. This has been worked out by us using the relativistic transport model based on the extended Walecka model [36], and was supported by the calculation of Cassing *et al* [37,38] using a dropping in-medium rho meson mass predicted from the QCD sum rules. As in hydrodynamical approaches [39], the starting point of Refs. [36] is the assumption that in the earlier stage of heavy-ion collisions a thermally equilibrated fire cylinder is formed. Although this is a reasonable approximation as it gives a satisfactory explanation for the observed particle yields and spectra from these collisions [44], a fully microscopic transport model including initial stage string dynamics is still desirable. Moreover, any ‘anomalous’ phenomena in heavy-ion collisions have to be discussed with respect to proton-induced reactions. Both the CERES and the HELIOS-3 collaboration have also measured dilepton production in proton-nucleus reactions, it is thus of interest to see if the data in proton-nucleus reactions can be explained in a ‘conventional’ way. This has not been possible in Ref. [36], as the fire cylinder model is not applicable to proton-induced reactions.

In Refs. [37,38], the Hadron-String Dynamics [45] has been used to study dilepton production from both proton-nucleus and nucleus-nucleus collisions. The conclusion from these studies is that although conventional mechanisms are sufficient to account for the dilepton spectra from proton-induced collisions, medium effects as that proposed in Ref. [36] are

needed to explain the enhanced low-mass dileptons in nucleus-nucleus collisions. In this paper, we carry out a similar calculation as in Refs. [36–38], but use initial hadron phase space distributions generated by string fragmentation in the initial stage of the relativistic quantum molecular dynamics (RQMD) [46,47]. It is worthwhile to mention that the RQMD model has been quite successful in describing many aspects of heavy-ion collisions at SPS/CERN energies.

This paper is organized as follows. In Section II, we discuss briefly the string dynamics for the initial stage of heavy-ion collisions and the hadronic rescattering in later stages. In Section III, we present the formulae for dilepton production from hadronic interactions and hadronic decay. The results for dilepton production in proton-nucleus collisions are presented in Section IV. In section V, we compare our results for S+Au and S+W collisions to the CERES and the HELIOS-3 data. The predictions for dilepton production in Pb+Au collisions will be discussed in Section VI. Finally a brief summary and outlook is given in Section VII.

## II. THE RELATIVISTIC TRANSPORT MODEL

The fragmentation of strings which may be viewed as an idealization of longitudinally stretched chromoelectric flux-tubes is a phenomenological approach to strong interactions which has been applied to multi-particle production in the soft regime for a long time [48,49]. String excitations are also an essential ingredient for recent microscopic approaches to ultrarelativistic nucleus-nucleus collisions, like e.g. RQMD [46,47]. Inelastic hadron-hadron collisions are described by forming strings from ingoing quarks and their primordial momenta. This concept is generalized to nuclear collisions by allowing for multiple collisions of a projectile with several target nucleons. As a new feature present only with nuclei as collision partners, RQMD includes the fusion of several overlapping strings into a ‘rope’, a flux-tube with larger than elementary color charge as the source. Created strings and ropes decay subsequently, because quark pairs are created and screen the initial fields. It is often

assumed that new hadrons are formed only after the two ingoing nuclei have passed through each other. This picture emerges also from the RQMD model at sufficiently high beam energies, because the typical times for hadron formation from string and rope fragmentation are getting larger than the passage time of the two Lorentz contracted nuclei.

From the RQMD model (version 2.1) we obtain the hadrons from the primary nucleon-nucleon collisions in the initial stage of heavy-ion collisions. These hadrons and their distributions in position and momentum space are then used as the input to the relativistic transport model [36]. When in-medium masses are used, both the yield and distribution of hadrons from string fragmentation may be different from that using the free masses [45]. Since the hadron abundance and distribution in heavy-ion collisions reach the equilibrium values very quickly as shown in our calculations, the results obtained in the following are thus not sensitive to the change of this initial distributions. We shall thus ignore such effects by using the same initial hadron abundance and spatial and momentum distributions whether the free or in-medium masses are used.

The treatment of subsequent hadronic rescattering in the relativistic transport model is similar to that in Ref. [36]. In the following, we mention briefly those processes that are directly relevant for dilepton production. For a pair of pions with a total invariant mass  $M$ , a rho meson of this mass is formed with an isospin-averaged cross section given by the Breit-Wigner form [22]

$$\sigma_{\pi\pi\rightarrow\rho}(M) = \frac{8\pi}{\mathbf{k}^2} \frac{(m_\rho\Gamma_\rho)^2}{(M^2 - m_\rho^2)^2 + (m_\rho\Gamma_\rho)^2} \left(\frac{M}{m_\rho}\right)^2, \quad (1)$$

where  $\mathbf{k}$  is the pion momentum in the center-of-mass frame of the rho meson. Similarly, for  $\pi\rho \rightarrow a_1$  the isospin-averaged cross sections [51] is

$$\sigma_{\pi\rho\rightarrow a_1}(M) = \frac{4\pi}{3\mathbf{k}^2} \frac{(m_{a_1}\Gamma_{a_1})^2}{(M^2 - m_{a_1}^2)^2 + (m_{a_1}\Gamma_{a_1})^2}, \quad (2)$$

The kaon-antikaon collision mainly proceeds through the formation and decay of a phi meson, with an isospin-averaged cross section given by

$$\sigma_{K\bar{K}\rightarrow\phi}(M) = \frac{3\pi}{\mathbf{k}^2} \frac{(m_\phi\Gamma_\phi)^2}{(M^2 - m_\phi^2)^2 + (m_\phi\Gamma_\phi)^2} \left(\frac{M}{m_\phi}\right)^2. \quad (3)$$

In treating meson decays we use the momentum-dependent decay width. For  $\rho \rightarrow \pi\pi$  and  $\phi \rightarrow K\bar{K}$ , they are given, respectively, by [22]

$$\Gamma_{\rho \rightarrow \pi\pi}(M) = \frac{g_{\rho\pi\pi}^2}{4\pi} \frac{(M^2 - 4m_\pi^2)^{3/2}}{12M^2}, \quad (4)$$

and

$$\Gamma_{\phi \rightarrow K\bar{K}}(M) = \frac{g_{\phi K\bar{K}}^2}{4\pi} \frac{(M^2 - 4m_K^2)^{3/2}}{6M^2}, \quad (5)$$

where  $g_{\rho\pi\pi}^2/4\pi \approx 2.9$  and  $g_{\phi K\bar{K}}^2/4\pi \approx 1.7$  are determined from the measured width at  $m_\rho$  and  $m_\phi$ , respectively. For the decay width of  $a_1 \rightarrow \pi\rho$ , we use the result of Ref. [51], i.e.,

$$\Gamma_{a_1 \rightarrow \pi\rho} = \frac{G_{a_1\pi\rho}^2 |\mathbf{k}|}{24\pi m_{a_1}^2} [2(p_\pi \cdot p_\rho)^2 + m_\rho^2(m_\pi^2 + |\mathbf{k}|^2)], \quad (6)$$

where  $\mathbf{k}$  is the pion momentum in the rest frame of  $a_1$ ;  $G_{a_1\pi\rho} \approx 14.8 \text{ GeV}^{-1}$  is determined from the  $a_1$  decay width in free space using its centroid mass. There is no simple expression for the decay width of  $\omega \rightarrow \pi^+\pi^-\pi^0$  [52], so we use the approximation that this width is proportional to the mass of omega meson. This approximation becomes exact in the chiral limit of  $m_\pi \rightarrow 0$ .

To study consistently the effects of dropping vector meson masses on the dilepton spectrum in heavy-ion collisions, we need a model for in-medium vector meson masses that can be incorporated into the relativistic transport model. In Ref. [36], this is achieved by extending the Walecka model [53] from the coupling of nucleons to scalar and vector fields to the coupling of light quarks to these fields, using the ideas of the meson-quark coupling model [30] and the constituent quark model. Here, we briefly review this model.

For a system of baryons (we take the nucleon as an example), pseudoscalar mesons ( $\pi$  and  $\eta$  mesons), vector mesons (rho and omega mesons), and the axial-vector meson ( $a_1$ ) at temperature  $T$  and baryon density  $\rho_B$ , the scalar field  $\langle S \rangle$  is determined self-consistently from

$$m_S^2 \langle S \rangle = \frac{4g_S}{(2\pi)^3} \int d\mathbf{k} \frac{m_N^*}{E_N^*} \left[ \frac{1}{\exp((E_N^* - \mu_B)/T) + 1} + \frac{1}{\exp((E_N^* + \mu_B)/T) + 1} \right]$$

$$\begin{aligned}
& + \frac{0.45g_S}{(2\pi)^3} \int d\mathbf{k} \frac{m_\eta^*}{E_\eta^*} \frac{1}{\exp(E_\eta^*/T) - 1} + \frac{6g_S}{(2\pi)^3} \int d\mathbf{k} \frac{m_\rho^*}{E_\rho^*} \frac{1}{\exp(E_\rho^*/T) - 1} \\
& + \frac{2g_S}{(2\pi)^3} \int d\mathbf{k} \frac{m_\omega^*}{E_\omega^*} \frac{1}{\exp(E_\omega^*/T) - 1} + \frac{6\sqrt{2}g_S}{(2\pi)^3} \int d\mathbf{k} \frac{m_{a_1}^*}{E_{a_1}^*} \frac{1}{\exp(E_{a_1}^*/T) - 1}, \quad (7)
\end{aligned}$$

where we have used the constituent quark model relations for the nucleon and vector meson masses [30], i.e.,

$$m_N^* = m_N - g_S \langle S \rangle, \quad m_\rho^* \approx m_\rho - (2/3)g_S \langle S \rangle, \quad m_\omega^* \approx m_\omega - (2/3)g_S \langle S \rangle, \quad (8)$$

and the quark structure of the  $\eta$  meson in free space which leads to

$$m_\eta^* \approx m_\eta - 0.45g_S \langle S \rangle, \quad (9)$$

and the Weinberg sum rule relation between the rho-meson and  $a_1$  meson masses [54,55], i.e,

$$m_{a_1}^* \approx m_{a_1} - (2\sqrt{2}/3)g_S \langle S \rangle. \quad (10)$$

In the calculation we use the scalar and vector coupling parameters of the original Walecka model that are fitted to the nuclear matter properties at normal density. In high-energy heavy-ion collisions, the system is not necessary in thermal and chemical equilibrium. The thermal distributions in Eq. (7) are thus replaced by the hadron momentum distributions in determining the scalar field.

### III. DILEPTON PRODUCTION: FORMALISM

The main contributions to dileptons with mass below 1.2 GeV are the Dalitz decay of  $\pi^0$ ,  $\eta$  and  $\omega$ , the direct leptonic decay of vector mesons such as  $\rho^0$ ,  $\omega$  and  $\phi$ , and the pion-pion annihilation which proceeds through the  $\rho^0$  meson, and the kaon-antikaon annihilation that proceeds through the  $\phi$  meson.

The Dalitz decay of  $\pi^0$ ,  $\eta$ , and  $\omega$  contributes significantly to dileptons with mass below  $2m_\pi$ . The differential width of Dalitz decay is related to its radiative decay width [56]. For pseudoscalar meson  $P$  (either  $\pi^0$ ,  $\eta^0$  or  $\eta'$ ), we have [56]

$$\begin{aligned} \frac{d\Gamma(P \rightarrow \gamma l^+ l^-)}{dM} &= \frac{4\alpha}{3\pi} \frac{\Gamma(P \rightarrow 2\gamma)}{M} \left(1 - \frac{4m_l^2}{M^2}\right)^{1/2} \\ &\times \left(1 + \frac{2m_l^2}{M^2}\right) \left(1 - \frac{M^2}{m_P^2}\right)^3 |F_P(M^2)|^2, \end{aligned} \quad (11)$$

where  $M$  is the mass of produced dilepton,  $\alpha$  is the fine structure constant,  $\Gamma(P \rightarrow 2\gamma)$  is the measured radiative decay width of a pseudoscalar meson [57], and  $m_l$  is the mass of the lepton. In the case of dielectron production,  $m_l = m_e \approx 0.51$  MeV can be neglected. The electromagnetic form factors of  $\pi^0$ ,  $\eta$  and  $\eta'$  are parameterized, respectively, as [56]

$$F_{\pi^0}(M^2) = 1 + b_{\pi^0} M^2, \quad (12)$$

$$F_{\eta}(M^2) = \left(1 - \frac{M^2}{\Lambda_{\eta}^2}\right)^{-1}, \quad (13)$$

$$F_{\eta'}(M^2) = \frac{m_{\rho}^4}{(M^2 - m_{\rho}^2)^2 + (m_{\rho}\Gamma_{\rho})^2}, \quad (14)$$

where  $b_{\pi^0} = 5.5$  GeV<sup>-2</sup>,  $\Lambda_{\eta} \approx 0.72$  GeV, and  $m_{\rho}$  and  $\Gamma_{\rho}$  are the mass and width of rho meson, respectively. These form factors describe reasonably well the empirical data [56].

For  $\omega \rightarrow \pi^0 l^+ l^-$ , the differential decay width is given by

$$\begin{aligned} \frac{d\Gamma(\omega \rightarrow \pi^0 l^+ l^-)}{dM} &= \frac{2\alpha}{3\pi} \frac{\Gamma(\omega \rightarrow \pi^0 \gamma)}{M} \left(1 - \frac{4m_l^2}{M^2}\right)^{1/2} \left(1 + \frac{2m_l^2}{M^2}\right) \\ &\times \left[ \left(1 + \frac{M^2}{m_{\omega}^2 - m_{\pi^0}^2}\right)^2 - \left(\frac{2m_{\omega} M}{m_{\omega}^2 - m_{\pi}^2}\right)^2 \right] |F_{\omega}(M^2)|^2, \end{aligned} \quad (15)$$

where  $\Gamma(\omega \rightarrow \pi^0 \gamma) = 0.717$  MeV is the omega meson radiative decay width [57]. In Ref. [56], the electromagnetic form factor was parameterized as

$$F_{\omega}(M^2) = \left(1 - \frac{M^2}{\Lambda_{\omega}^2}\right)^{-1}, \quad (16)$$

with  $\Lambda_{\omega} = 0.65$  GeV, somewhat smaller than  $m_{\rho}$ , indicating the deviation from the vector dominance model.

The treatment of  $a_1$  Dalitz decay is slightly different. Since in our dynamical model the processes  $a_1 \leftrightarrow \pi\rho$  and  $\rho \rightarrow l^+ l^-$  are treated explicitly, we have already included that part of  $a_1$  contribution to dileptons which proceeds through a physical  $\rho$  meson as a two-step

process. Thus, in evaluating the  $a_1$  Dalitz decay ( $a_1 \rightarrow \pi^+ l^-$ ) we do not need to introduce the vector-dominance model form factor. Otherwise, there would be double counting.

The direct leptonic decay of vector mesons is another important source of dileptons. For dileptons of mass in the region of interest to this work, we consider mainly the leptonic decay of  $\rho^0$ ,  $\omega$  and  $\phi$  mesons. The decay width for  $\rho^0 \rightarrow l^+ l^-$  is given by

$$\begin{aligned}\Gamma_{\rho^0 \rightarrow l^+ l^-}(M) &= \frac{g_{\rho\gamma}^2 e^2 M}{M^4} \frac{1}{3} \left(1 - \frac{4m_l^2}{M^2}\right)^{1/2} \left(1 + \frac{2m_l^2}{M^2}\right) \\ &= \frac{\alpha^2}{(g_{\rho\pi\pi}^2/4\pi)} \frac{m_\rho^4}{3M^3} \left(1 - \frac{4m_l^2}{M^2}\right)^{1/2} \left(1 + \frac{2m_l^2}{M^2}\right),\end{aligned}\quad (17)$$

where  $M^4$  in the denominator arises from the virtual photon propagator and  $M$  in the numerator comes from the phase space integration. In obtaining the second expression, we have used the vector dominance relation  $g_{\rho\gamma} = em_\rho^2/g_{\rho\pi\pi}$  [58]. Using  $g_{\rho\pi\pi}^2/4\pi \approx 2.9$  in Eq.(17), we get  $\Gamma_{\rho^0 \rightarrow e^+ e^-} \approx 5$  keV, and this is somewhat different from the measured width of 6.5 keV, indicating the breaking of universal vector coupling. In the calculation, we use instead

$$\Gamma_{V \rightarrow e^+ e^-}(M) = C_{e^+ e^-} \frac{m_V^4}{M^3}, \quad (18)$$

$$\Gamma_{V \rightarrow \mu^+ \mu^-}(M) = C_{\mu^+ \mu^-} \frac{m_V^4}{M^3} \left(1 - \frac{4m_\mu^2}{M^2}\right)^{1/2} \left(1 + \frac{2m_\mu^2}{M^2}\right), \quad (19)$$

where  $V$  stands for  $\rho^0$ ,  $\omega$ , or  $\phi$ . The coefficient  $C_{e^+ e^-}$  in the dielectron channel is  $8.814 \times 10^{-6}$ ,  $0.767 \times 10^{-6}$ , and  $1.344 \times 10^{-6}$  for  $\rho^0$ ,  $\omega$ , and  $\phi$  decay, respectively, which are determined from the measured width [57]. Similarly, from the measured width of decaying into dimuons, we determine the coefficient  $C_{\mu^+ \mu^-}$  to be  $9.091 \times 10^{-6}$  and  $1.071 \times 10^{-6}$  for  $\rho^0$  and  $\phi$  decay, respectively. For  $\Gamma_{\omega \rightarrow \mu^+ \mu^-}$ , only an upper bound is given in the particle data book [57]; we assume that this width is the same as that for the dielectron channel. Our fit to HELIOS-3 data for p+W collisions shows that this is a good approximation (see Fig. 3 below).

The formation of an omega meson from the three-pion interaction is neglected. In this calculation, all omega mesons are thus from the initial stage of heavy-ion collisions through string fragmentation. For rho and phi mesons we include also secondary processes such as

pion-pion annihilation and kaon-antikaon annihilation, in addition to primary production from string fragmentation. The contribution of pion-pion and kaon-antikaon annihilation to dilepton production, which have been known to be important for heavy-ion collisions, is therefore treated as a two-step process with the explicit intermediate vector meson formation, propagation, and decay. It can be easily shown that the product of the rho meson formation cross section, Eq. (1), and the branching ratio,  $\Gamma_{\rho^0 \rightarrow l^+ l^-} / \Gamma_\rho$ , for the rho meson to decay into dilepton leads to a dilepton production cross section that is the same as that from pion-pion annihilation in the usual form factor approach [14,22], i.e.,

$$\sigma_{\pi^+ \pi^- \rightarrow \rho^0 \rightarrow l^+ l^-} = \frac{8\pi\alpha^2 k}{3M^3} \frac{m_\rho^4}{(M^2 - m_\rho^2)^2 + (m_\rho \Gamma_\rho)^2} \left(1 - \frac{4m_l^2}{M^2}\right)^{1/2} \left(1 + \frac{2m_l^2}{M^2}\right). \quad (20)$$

The same relation holds for dileptons from kaon-antikaon annihilation. The interaction of a pion and a rho meson dominantly produces an  $a_1$ , and their contribution to dilepton production is thus included in our model through  $a_1$  Dalitz decay.

It should be mentioned that when medium effects on vector meson masses are included,  $m_\rho$ ,  $m_\omega$ , and  $m_\phi$  in the above expressions are replaced by  $m_\rho^*$ ,  $m_\omega^*$ , and  $m_\phi^*$ , respectively. Also, the in-medium decay widths are used in these expressions, and they are calculated from Eqs. (4-6) with in-medium masses. As in Ref. [36], we have neglected the collisional broadening of vector meson widths in medium [59], based on the argument that their magnitudes are comparable to the mass resolution in CERES experiments, so they do not affect appreciably the final results.

In our model, dileptons are emitted continuously during the time evolution of the colliding system. The way the dilepton yield is calculated can be illustrated by rho meson decay. Denoting, at time  $t$ , the differential multiplicity of neutral rho mesons by  $dN_{\rho^0}(t)/dM$ , then the differential dilepton production probability is given by

$$\frac{dN_{l^+ l^-}}{dM} = \int_0^{t_f} \frac{dN_{\rho^0}(t)}{dM} \Gamma_{\rho^0 \rightarrow l^+ l^-}(M) dt + \frac{dN_{\rho^0}(t_f)}{dM} \frac{\Gamma_{\rho^0 \rightarrow l^+ l^-}(M)}{\Gamma_\rho(M)}, \quad (21)$$

where  $t_f$  is the freeze-out time, which is found to be about 20 fm/c. The first term corresponds to dilepton emission before freeze out while the second term is from decay of rho mesons still present after freeze out.

#### IV. DILEPTON PRODUCTION: PROTON-NUCLEUS REACTIONS

As already mentioned in the introduction, any ‘anomalous’ phenomena in heavy-ion collisions need to be compared with proton-induced reactions. In order to claim that the CERES and HELIOS-3 dilepton data as indications of medium effects in heavy-ion collisions, it is necessary that we can describe the dilepton data in proton-nucleus collisions with the ‘conventional’ mechanism. In these reactions, dileptons are expected to be produced outside the nucleus due to finite formation time, so no ‘exotic’ phenomena are expected to happen when compared to dilepton production from the proton-proton interaction.

The results for dilepton spectra from p+Be collisions at 450 GeV are shown in Fig. 1, together with the data from the CERES collaboration [34]. It is seen that the data can be well reproduced by the Dalitz decay of  $\pi^0$ ,  $\eta$  and  $\omega$  mesons, and the direct leptonic decay of  $\rho^0$ ,  $\omega$  and  $\phi$  mesons. These results are thus similar to that found in Refs. [37] using the Hadron-String Dynamics, and are also similar to the ‘cocktail’ constructed by the CERES collaboration from known and expected sources of dileptons [34]. We see that very low mass dileptons are mainly from the Dalitz decay of  $\pi^0$  and are strongly suppressed by experimental acceptance cuts in the opening angle and transverse momentum. Dileptons in the mass region from 0.15 to 0.45 GeV are mainly from  $\eta$  meson Dalitz decay. Around  $m_{\rho,\omega}$ , the contribution from  $\omega$  decay is more important than that from  $\rho^0$  decay, as the latter has a very broad mass distribution. Dileptons with mass around 1 GeV are mainly due to  $\phi$  meson decay.

A similar comparison with the CERES data for p+Au collisions at 450 GeV is given in Fig. 2. Again, the data are very well reproduced by conventional sources of Dalitz decay and direct vector meson decay. Comparing Fig. 1 with Fig. 2 we see that both the experimental data and our theoretical results are essentially the same in the two collisions, so there is no discernible difference in the dilepton spectra in going from an extremely light Be target (which is similar to proton-proton interactions) to a much heavier Au target.

The comparison with the HELIOS-3 dimuon data from p+W collisions at 200 GeV is

presented in Fig. 3. Up to dimuon mass of about 1.3 GeV, the data are again very well explained by the Dalitz decay of  $\eta$  and  $\omega$  and the direct vector meson decay of  $\rho^0$ ,  $\omega$  and  $\phi$ . The low mass dimuons are mainly from the  $\eta$  Dalitz decay, while the  $\omega$  meson Dalitz decay is important in the mass range of 0.4 to 0.6 GeV. As in the CERES case, the contribution from the  $\omega$  decay is more important than that from the  $\rho^0$  around  $m_{\rho,\omega}$ . Both the CERES and the HELIOS-3 data for dilepton production in proton-nucleus reactions are thus consistent with each other, in spite of quite different experimental setups and acceptance cuts.

## V. DILEPTON PRODUCTION: NUCLEUS-NUCLEUS COLLISIONS

Comparing the experimental data from nucleus-nucleus collisions to those from proton-nucleus collisions, both the CERES and the HELIOS-3 collaboration have found substantial enhancement of low-mass dileptons in the mass region from about  $2m_\pi$  to about 0.6 GeV, which cannot be explained by uncertainties and errors of the normalization procedure [60]. In going from proton-induced reactions to heavy-ion collisions, the main difference is additional contributions from pion-pion and kaon-antikaon annihilation to dilepton production in heavy-ion collisions. If the observed enhancement of low-mass dileptons can be explained by pion-pion annihilation, it is fine but cannot be considered as an ‘anomaly’, as the importance of pion-pion annihilation has already been seen in the DLS data [31]. However, as shown in Refs. [36–38] and will be shown in this Section, including the contribution from pion-pion annihilation but without any medium effects, the theoretical results in the low-mass region are still significant below both the CERES and HELIOS-3 data.

### A. CERES: S+Au collisions

We first show in Fig. 4 the initial pion and proton rapidity distributions and transverse momentum spectra obtained in the RQMD for central S+Au collisions at 200 GeV/nucleon and impact parameter  $b \leq 3$  fm, corresponding to a final charged particle multiplicity of  $dN_{ch}/d\eta \approx 125$  in the rapidity range  $2.1 < \eta < 2.65$  as in the CERES experiments. Also

shown is the time evolution of central baryon density. For comparison, the initial conditions and time evolution of the central density used in the fire cylinder model of Ref. [36] are also shown. It is seen that the two initial conditions agree reasonably with each other. Initially, the slope parameter of the pion transverse mass distribution is about 165 MeV, the average baryon density in the central region is about  $2.3 \rho_0$ , and the average energy density is about  $2.5 \text{ GeV}/\text{fm}^3$ . In Fig. 5, we show the time evolution of the abundance of both participant baryons and produced mesons. We note that initially the pion number is about twice the rho meson number, and the omega meson number is about  $1/3$  of the rho meson number. In the free meson mass case, rho mesons are seen to continuously decay, leading to an increase of the pion number. The number of higher baryon resonances, whose in-medium masses are always used in the relativistic transport model, increases initially as their number is below the equilibrium one. After reaching the equilibrium value, it starts to decrease as the system expands. When in-medium meson masses are introduced in the model, the time evolution of the baryon abundance remains similar as their in-medium masses are essentially the same. However, the time evolution of the rho meson number changes to the one like the higher baryon resonances, indicating that initially their number is below the equilibrium value due to a smaller mass in medium.

After following the time evolution of the colliding system using the relativistic transport model, hadronic observables can be calculated. In Fig. 6, we show the final rapidity distributions of negatively-charged hadrons (mainly  $\pi^-$  and  $K^-$ ) and protons together with the experimental data from the NA35 collaboration [61] and the NA44 collaboration [62]. Compared with that in Ref. [36], we see a significant improvement of agreements between the theoretical results with the data in the backward rapidity region. The comparison of transverse mass spectra of protons and pion in mid- to forward-rapidity region with experimental data for a similar system S+Pb from the NA44 collaboration [62] is shown in Fig. 7. Overall, the theoretical results agree well with the data.

Also of interest is the  $\eta/\pi^0$  ratio in these collisions. The WA80 collaboration has recently published their measurement of this quantity for minimum-biased events [63]. Some very

preliminary data with large error bars were reported in Ref. [64] for central collisions. The comparison of our theoretical results with the WA80 data is shown in Fig. 8. Our  $\eta/\pi^0$  ratio is larger than the minimum-biased data (solid circles), but somewhat smaller than the central collision data (solid squares), especially in the low transverse momentum region. We believe that our results correspond reasonably to the ratio in CERES experiments, as less central events are selected in CERES experiments than in WA80 experiments, which has an average charged-particle multiplicity density of more than 160 in the same rapidity region [64,65].

With free meson masses, the calculated dilepton spectra, normalized by the average charged-particle multiplicity, are shown in Fig. 9 together with the CERES data. As in the case of proton-nucleus reactions, dileptons with mass below 0.1 GeV are mainly from  $\pi^0$  Dalitz decay. The  $\eta$  Dalitz decay is important in the mass range from 0.15 to 0.35 GeV. From 0.35 to 0.7 GeV, dileptons are mainly from pion-pion annihilation through  $\rho^0$  meson. Contrary to the observation in proton-nucleus reactions where the  $\omega$  decay is more important around  $m_{\rho,\omega}$ , in S+Au collisions the contribution from  $\rho^0$  decay becomes more important when free meson masses are used. This is mainly due to an enhanced rho contribution from pion-pion annihilation in heavy-ion collisions. A bump around 0.7 GeV in the dilepton spectrum from  $\eta'$  meson decay is a result of the vector meson dominance form factor in Eq. (14). There should have appeared a similar bump in the contribution from  $a_1$  Dalitz decay if we had included the vector meson dominance form factor rather than treated it as a two-step process in the rho meson mass region.

The importance of pion-pion annihilation in the low-mass region, as emphasized by the CERES collaboration [34], can be more clearly seen in Fig. 10, where the CERES data are compared with theoretical results calculated with and without the contribution from pion-pion annihilation. Without pion-pion annihilation, the theoretical results for dileptons with invariant mass from 0.3 to 0.65 GeV are significantly reduced, and the disagreement with the experimental data becomes comparable to that found by the CERES collaboration based on known and expected sources [34].

The inclusion of pion-pion annihilation, though found to be quite important in the mass region of interest, still does not give enough number of dileptons in the mass region from 0.25 to 0.6 GeV. Furthermore, for dileptons with mass around  $m_{\rho,\omega}$  there are more dileptons predicted by the theoretical calculations than shown in the experimental data. This is very similar to our earlier results based on a thermally equilibrated fire cylinder model [36]. These results are also similar to those of Cassing *et al* [37] based on the Hadron-String Dynamics model and Srivastava *et al* [39] based on the hydrodynamical model, as shown in Fig. 11. We note that a strong peak around  $m_\phi$  in the results of Srivastava *et al* will become a bump once the mass resolution of the CERES collaboration is properly included.

The failure of these models with free meson masses in explaining the CERES data has led to the suggestion that medium modifications of vector meson masses are needed as shown in Refs. [22,37,38]. The comparison of our results obtained with in-medium meson masses with the CERES data is shown in Fig. 12. We have about a factor of 2-3 enhancement of the dilepton yield in the mass range from 0.2 to 0.6 GeV, as compared with the results obtained with free meson masses. Overall, the agreement with the CERES data becomes much better with the use of in-medium vector meson masses. These results are again very similar to those in Ref. [36] obtained in the fire-cylinder model.

### B. HELIOS-3: S+W collisions

The same model has been used to calculate the dimuon spectra from central S+W collisions by the HELIOS-3 collaboration. The results obtained with free meson masses are shown in Fig. 13. As in proton-induced reactions, dimuons with mass below 0.3 GeV are from  $\eta$  meson Dalitz decay. From 0.35 to 0.55 GeV, the  $\omega$  meson Dalitz decay is important. In heavy-ion collisions, the contribution from  $\rho^0$  decay becomes important due to pion-pion annihilation. However, the role of pion-pion annihilation in HELIOS-3 experiments is less significant than that in CERES experiments, as HELIOS-3 measures dileptons in the forward rapidity region which has a smaller charged-particle multiplicity than that in the

mid-rapidity region measured by CERES.

With free meson masses, the theoretical results are below the HELIOS-3 data in the mass region from 0.35 to 0.6 GeV, and slightly above the data around  $m_{\rho,\omega}$ . Qualitatively, this is similar to the situation in the CERES case, but quantitatively, the discrepancy between the theory and the data is somewhat smaller in the HELIOS-3 case. For example, for the CERES data the theoretical results underpredicts most significantly around 0.4 GeV and are below the data by about a factor of 4, while for the HELIOS-3 data this happens around 0.5 GeV, and the theoretical prediction is below the data by less than a factor of two. In other words, the enhancement of low-mass dileptons is less pronounced in the HELIOS-3 than in the CERES experiments. This is again due to the fact that the HELIOS-3 measures dileptons in the forward rapidity region with a smaller charged-particle multiplicity than in the CERES experiments.

Our results obtained with in-medium meson masses are shown in Fig. 14. Again, we see enhanced dilepton yield in the low mass region, and a reduction around  $m_{\rho,\omega}$ , as compared to the results obtained with free meson masses. This brings the theoretical results in better agreement with the data. The importance of in-medium meson masses in explaining the HELIOS-3 data has also been found by Cassing *et al* [38].

For dimuon spectra in p+W collision up to 1.3 GeV, the HELIOS-3 data can be well described by the Dalitz decays and direct vector meson decay. For S+W collisions, the HELIOS-3 data above 1.2 GeV are grossly underestimated by theoretical calculations with both free and in-medium vector meson masses. The enhancement of dilepton production in heavy-ion collisions in this intermediate mass region indicates that thermal processes such as  $\pi a_1 \rightarrow l^+ l^-$  [66] and the decay of heavier vector mesons such as  $\omega(1390)$  [67,68] might become important. Also, contributions from the quark-gluon plasma and the initial Drell-Yan processes may not be negligible.

## VI. DILEPTON PRODUCTION: PREDICTIONS FOR Pb+Au COLLISIONS

Dilepton production in Pb+Au collisions at 160 GeV/nucleon is currently being measured by the CERES collaboration. Based on the model outlined above, which has been successful in explaining both the CERES and HELIOS-3 data with reduced vector meson masses in hot and dense matter, we present our predictions for dilepton spectra from this collision using current CERES mass resolution and acceptance cuts for S+Au collisions.

We first consider central Pb+Au collisions. In Fig. 15, we show the initial pion and proton rapidity and transverse mass distributions as well as the time evolution of baryon density in this collision. Initially, the pion transverse slope parameter is about 190 MeV, the average baryon density is about  $4 \rho_0$ , and the average energy density is about 3.3 GeV/fm<sup>3</sup>. These initial parameters are somewhat higher than in S+Au collisions at 200 GeV/nucleon. As in Ref. [36], the system expands slightly slower in the case of dropping meson masses. The time evolution of the abundance of participant baryons and produced mesons is shown in Fig. 16 for both free and in-medium meson masses. As in S+Au collisions, the initial pion number is about twice of that of rho mesons, and the omega number is about 1/3 of the rho meson number. For the case of free meson masses, the time dependence of the particles is similar to what we see in the S+Au collision. Introducing in-medium meson masses gives a similar time dependence of the meson abundance as in the S+Au collision with in-medium masses. However, a peculiar behavior of the baryon abundance occurs at about 3 fm/c after the expansion, when baryon resonances are reformed after initial decays, and this is not seen in S+Au collisions. We believe that this is due to the larger  $\pi/N^*$  ratio in Pb+Au collisions ( $\approx 15$  at  $t=3$  fm/c) than in S+Au collisions ( $\approx 4$  at the same time), which thus favors the formation of baryon resonances in the Pb collision.

For central Pb+Au and Pb+Pb collisions some preliminary data for the charged-particle rapidity distribution and transverse mass spectra have become available from the NA49 and the NA44 collaboration. We compare in Fig. 17 the calculated negatively-charged particle (mainly  $\pi^-$  and  $K^-$ ) rapidity distribution with preliminary data from the NA49 collabora-

tion [61]. The agreement with the data is fairly good. Also shown in Fig. 17 is the final proton rapidity distribution, which shows more appreciable stopping than in S+Au collisions. The nucleon to pion ratio in the mid-rapidity is still about 0.15 as in S+Au collisions. The final proton rapidity distribution is somewhat different from the initial one from string fragmentation (see upper left panel of Fig. 15). Because of longitudinal expansion, a hole is seen to develop in the mid-rapidity. We note that in our initial proton rapidity distribution hyperons have not been included, while our final proton rapidity distribution (lower panel of Fig. 17) includes also the protons from hyperon decay. The calculated final proton and pion transverse momentum spectra agree with the preliminary data from the NA44 collaboration [62] as shown in Fig. 18.

The theoretical predictions for the dielectron spectra in central Pb+Au collisions with CERES mass resolution and acceptance cuts are given in Fig. 19(a) for the two scenarios of free meson masses and in-medium meson masses. The normalization factor  $dN_{ch}/d\eta$  here is the average charge particle pseudo-rapidity density in the pseudo-rapidity range 2 to 3, and is about 440 in this collision. With free meson masses, we see a strong peak around  $m_{\rho,\omega}$ , which is dominated by  $\rho^0$  meson decay as a result of an enhanced contribution from pion-pion annihilation in Pb+Au collisions than in S+Au and proton-nucleus collisions. With in-medium meson masses, the  $\rho$  meson peak shifts to a lower mass, and the peak around  $m_{\rho,\omega}$  becomes a shoulder arising mainly from  $\omega$  meson decay. At the same time we see an enhancement of low-mass dileptons in the region of 0.25-0.6 GeV as in S+Au collisions.

Since the maximum baryon density reached in heavy-ion collisions decreases with the impact parameter, we expect a decrease of medium effects on the dilepton spectrum at large impact parameters. Experimentally, this effect can be studied by measuring the dependence of the dilepton spectrum on the charged particle multiplicity. We have thus calculated the dilepton spectrum from Pb+Au collisions at 160 GeV/nucleon for a number of impact parameters. In Fig. 20, we show the impact parameter dependence of the initial average baryon density  $\rho/\rho_0$ , the final total negatively-charged particle multiplicity  $N_{ch}^-$ , and the average charge particle pseudorapidity density at midrapidity  $dN_{ch}^-/d\eta$ . Apparently, both

decrease with increasing impact parameter; the initial baryon density goes from about  $4\rho_0$  at  $b=0$  fm to  $1.9\rho_0$  at 9 fm, and  $N_{ch}^-$  decreases from about 820 at  $b=0$  fm to about 206 at  $b=9$  fm.

For both Dalitz decay and vector meson decay, the ratio of total number of dileptons (without acceptance cut) to the total negatively-charged hadron multiplicity  $N_{ch}^-$  as a function of  $N_{ch}^-$  are shown in Fig. 21. It is seen that in both free and in-medium meson mass cases, the dilepton yield from Dalitz decay increases linearly with the charge particle multiplicity, so the normalized yield is almost a constant. On the other hand, the dilepton yield from vector meson decay increases more than linearly due to contributions from pion-pion and kaon-antikaon annihilation. If we express  $N_{ee} \propto (N_{ch}^-)^\alpha$ , then our results show that  $\alpha \approx 1.3$  for the case of free meson masses and  $\alpha \approx 1.5$  for the case of in-medium meson masses. The stronger dependence on the charged particle multiplicity in the latter case is due to the stronger medium effects in central collisions.

Finally, the calculated dilepton spectra from Pb+Au collisions at three different impact parameters of  $b=3, 6,$  and 9 fm are shown in Fig. 19(b), 19(c), and 19(d). The enhancement of low-mass dileptons are seen to decrease with increasing impact parameter.

## VII. SUMMARY AND OUTLOOK

In summary, we have studied in detail dilepton production from both proton-nucleus and nucleus-nucleus collisions using the relativistic transport model with initial conditions determined by the string fragmentation from the initial stage of the RQMD model.

We have found that the dilepton spectra in proton-nucleus reactions measured by the CERES and the HELIOS-3 collaboration can be well understood in terms of conventional mechanisms of Dalitz decay and direct vector meson decay.

For dilepton spectra in central S+Au and S+W collisions, these conventional mechanisms, however, fail to explain the data, especially in the low-mass region from about 0.25 to about 0.6 GeV in CERES experiments, and from 0.35 to 0.65 GeV in HELIOS-3 ex-

periments. Including the contribution from pion-pion annihilation, which is known to be important in the mass region from  $2m_\pi$  to  $m_{\rho,\omega}$ , removes some of the discrepancy. But the data in the low mass region are still substantially underestimated, and that around  $m_{\rho,\omega}$  somewhat overestimated by theoretical calculations. The agreement with the data is significantly improved when reduced in-medium vector meson masses are taken into account. The results of the present study based on initial conditions from the RQMD model is thus very similar to our earlier results assuming that initially there is a thermally equilibrated fire-cylinder.

We have also presented predictions for the dilepton spectra from central Pb+Au collisions. With an increased pion density in Pb+Au than in Sulfur-induced collisions, the dilepton yield from Dalitz decay and  $\omega$  decay increases roughly linearly with the charged-particle multiplicity, whereas the contribution from pion-pion annihilation increases more than linearly. This leads to some differences between the dilepton spectra from Pb+Au and Sulfur-induced collisions. We have also studied the impact parameter dependence of dilepton production in Pb+Au collisions, and found that the enhancement of low-mass dilepton decreases with increasing impact parameter. It would be very interesting to carry out experiments in which different centrality bins are selected so that this impact parameter dependence can be tested.

We thank W. Cassing, A. Drees, I. Kralik, M. Murray, I. Tserruya, and T. Ullrich, and P. Wurm for helpful communications. We are also very grateful to K. Wolf for providing us computing resources and for useful discussions. GQL and CMK were supported by the National Science Foundation under Grant No. PHY-9509266, and GEB and HS were supported by the Department of Energy under Grant No. DE-FG02-88ER40388.

## REFERENCES

- [1] For example, Quark Matter'95, Nucl. Phys. **A590**, (1995); Quark Matter'93, Nucl. Phys. **A566**, (1993).
- [2] E. Feinberg, Nuovo Cimento, **A34**, 39 (1976).
- [3] E. V. Shuryak, Phys. Lett. B **78**, 150 (1978); Phys. Rep. **67**, 71 (1980).
- [4] S. A. Chin, Phys. Lett. B **119**, 51 (1982).
- [5] G. Domokos, Phys. Rev. D **28**, 123 (1983).
- [6] L. D. McLerran and T. Tiomela, Phys. Rev. D **31**, 545 (1985).
- [7] K. Kajantie, J. Kapusta, L. McLerran, and A. Mekjian, Phys. Rev. D **34**, 2746 (1986).
- [8] C. M. Ko and L. H. Xia, Phys. Rev. Lett. **62**, 1595 (1989).
- [9] M. Asakawa and C. M. Ko, Phys. Lett. B322 , 33 (1994).
- [10] J. Cleymans, K. Redlich and H. Satz, Z. Phys. C **52**, 517 (1991).
- [11] P. V. Ruuskanen, Nucl. Phys. **A544**, 169c (1992); in *Particle production in highly excited matter*, ed. H. H. Gutbrod (Plenum, New York, 1993).
- [12] M. Asakawa, C. M. Ko, and P. Lévai, Phys. Rev. Lett. **70**, 398 (1993).
- [13] R. Vogt, S. J. Brodsky, and P. Hoyer, Nucl. Phys. **B383**, 643 (1992).
- [14] C. Gale and J. Kapusta, Phys. Rev. C **35**, 2107 (1987); C **38**, 2657 (1988).
- [15] L. H. Xia, C. M. Ko, L. Xiong, and J. Q. Wu, Nucl. Phys. **A485**, 721 (1988).
- [16] Gy. Wolf, W. Cassing, and U. Mosel, Nucl. Phys. **A552**, 549 (1993).
- [17] R. Pisarski, Phys. Lett. 110B, 155 (1982).
- [18] V. Koch, in *Proceedings of Pittsburgh Workshop on Soft Lepton Pair and Photon Production*, ed. J. A. Thompson, (Nova Science Publishers, New York, 1992), p. 251.

- [19] F. Karsch, K. Redlich and L. Turko, Z. Phys. C **60**, 519 (1993).
- [20] T. Hatsuda, Y. Koike and S. H. Lee, Nucl. Phys. **B394**, 221 (1993).
- [21] M. Hoffman, *et al.*, Nucl. Phys. **A566**, 15c (1994).
- [22] G. Q. Li and C. M. Ko, Nucl. Phys. **A582**, 731 (1995).
- [23] G. E. Brown and M. Rho, Phys. Rev. Lett. **66**, 2720 (1991).
- [24] C. Adami and G. E. Brown, Phys. Rep. **224**, 1 (1993).
- [25] T. Hatsuda and S. H. Lee, Phys. Rev. C **46**, R34 (1992).
- [26] M. Asakawa and C. M. Ko, Phys. Rev. C **48**, R526 (1993).
- [27] H. C. Jean, J. Piekarewicz, and A. G. Williams, Phys. Rev. C **49**, 1891 (1994).
- [28] H. Shiomi and T. Hatsuda, Phys. Lett. B **334**, 281 (1994).
- [29] C. S. Song, P. W. Xia, and C. M. Ko, Phys. Rev. C **52**, 408 (1995).
- [30] K. Saito and A. W. Thomas, Phys. Rev. C **51**, 2757 (1995).
- [31] G. Roche *et al.*, Phys. Rev. Lett. **61**, 1069 (1988);  
C. Naudet *et al.*, Phys. Rev. Lett. **62**, 2652 (1988).
- [32] L. Xiong, Z. G. Wu, C. M. Ko, and J. Q. Wu, Nucl. Phys. **A552**, 772 (1990).
- [33] W. Koenig, in *Proc. Workshop on dilepton production in relativistic heavy-ion collisions*, ed. H. Bokemeyer (GSI, Darmstadt, 1994).
- [34] G. Agakichiev *et al.*, Phys. Rev. Lett. **75**, 1272 (1995);  
J. P. Wurm for the CERES Collaboration, Nucl. Phys. **A590**, 103c (1995);  
A. Drees for the CERES/NA44 Collaboration, in *Proc. International Workshop XXIII on Gross Properties of Nuclei and Nuclear Excitations*, Ed. H. Feldmeier and W. Nörenberg, (GSI, Darmstadt, 1995) p. 151;

- [35] M. Maserà for the HELIOS-3 Collaboration, Nucl. Phys. **A590**, 93c (1995);  
I. Králik for the HELIOS-3 Collaboration, in *Proc. International Workshop XXIII on Gross Properties of Nuclei and Nuclear Excitations*, Ed. H. Feldmeier and W. Nörenberg, (GSI, Darmstadt, 1995) p. 143.
- [36] G. Q. Li, C. M. Ko, and G. E. Brown, Phys. Rev. Lett. **75**, 4007 (1995); Nucl. Phys. **A606** (1996) 568.
- [37] W. Cassing, W. Ehehalt, and C. M. Ko, Phys. Lett. B **363**, 35 (1995).
- [38] W. Cassing, W. Ehehalt, and I. Kralik, Phys. Lett. B **377**, 5 (1996).
- [39] D. K. Srivastava, B. Sinha, and C. Gale, Phys. Rev. C **53**, R567 (1996).
- [40] Z. Huang and X. N. Wang, Phys. Rev. D **53**, 5034 (1996).
- [41] J. Kapusta, D. Kharzeev, and L. McLerran, Phys. Rev. **D53**, 5028 (1996).
- [42] R. Rapp, G. Chanfray, and J. Wambach, Phys. Rev. Lett. **76**, 368 (1996).
- [43] V. Koch and C. Song, Phys. Rev. C **54** (1996) 1903
- [44] P. Braun-Munzinger, J. Stachel, J. Wessels, and N. Xu, Phys. Lett. B **365**, 1 (1996).
- [45] W. Ehehalt and W. Cassing, Nucl. Phys. **A602**, 449 (1996).
- [46] H. Sorge, H. Stöcker, and W. Greiner, Ann. Phys. **192**, 266 (1989).
- [47] H. Sorge, Phys. Rev. C **52**, 3291 (1995); Phys. Lett. B **373**, 16 (1996).
- [48] B. Andersson, G. Gustafson, G. Ingelman, and T. Sjöstrand, Phys. Rep. **97**, 31 (1983);  
T. Sjöstrand, Comp. Phys. Comm. **39**, 347 (1986).
- [49] B. Andersson, G. Gustafson, and B. Nilsson-Almqvist, Nucl. Phys. **B281**, 289 (1987);  
B. Nilsson-Almqvist and E. Stenlund, Comp. Phys. Comm. **43**, 387 (1987).
- [50] R. D. Field and R. P. Feynman, Nucl. Phys. **B136**, 1 (1978).

- [51] L. Xiong, E. Shuryak, and G. E. Brown, Phys. Rev D **46**, 3789 (1992).
- [52] O. Kaymakcalan, S. Rajeev, and J. Schechter, Phys. Rev. D **30**, 594 (1984).
- [53] B. D. Serot and J. D. Walecka, Adv. Nucl. Phys. **16**, 1 (1986).
- [54] S. Weinberg, Phys. Rev. Lett. **18**, 507 (1967).
- [55] J. I. Kapusta and E. V. Shuryak, Phys. Rev. D **49**, 4694 (1994).
- [56] L. G. Landberg, Phys. Rep. **128**, 301 (1985).
- [57] Particle Data Group, Review of Particle Properties, Phys. Rev. D **50**, 1173 (1994).
- [58] R. K. Bhaduri, Models of the Nucleon, (Addison-Wesley, Reading, MA, 1988).
- [59] K. Haglin, Nucl. Phys. **A584** (1995) 719.
- [60] I. Tserruya, Nucl. Phys. **A590**, 127c (1995).
- [61] D. Röhrlich for the NA35 collaboration, Nucl. Phys. **A566**, 35c (1994);  
M. Gazdzicki for the NA49 collaboration, Nucl. Phys. **A590**, 197c (1995).
- [62] M. Murray for the NA44 collaboration, in *Proc. Strangeness in Hadronic Matter*, ed. J. Rafelski (AIP, New York, 1995) p.162;  
B. V. Jacak for the NA44 collaboration, Nucl. Phys. **A590**, 215c (1995);  
J. Dodd for the NA44 collaboration, Nucl. Phys. **A590**, 523c (1995).
- [63] R. Albrecht *et al.*, Phys. Lett. B **361**, 14 (1995).
- [64] A. Lebedev *et al.*, Nucl. Phys. **A566**, 355c (1994).
- [65] R. Albrecht *et al.*, Z. Phys. C **50**, 539 (1992).
- [66] C. Song, C. M. Ko, and C. Gale, Phys. Rev. D **50**, R1827 (1994).
- [67] C. Gale and P. Lichard, Phys. Rev. D **49**, 3338 (1994).
- [68] K. Haglin and C. Gale, Phys. Rev. D **52**, 6297 (1995).

FIGURES

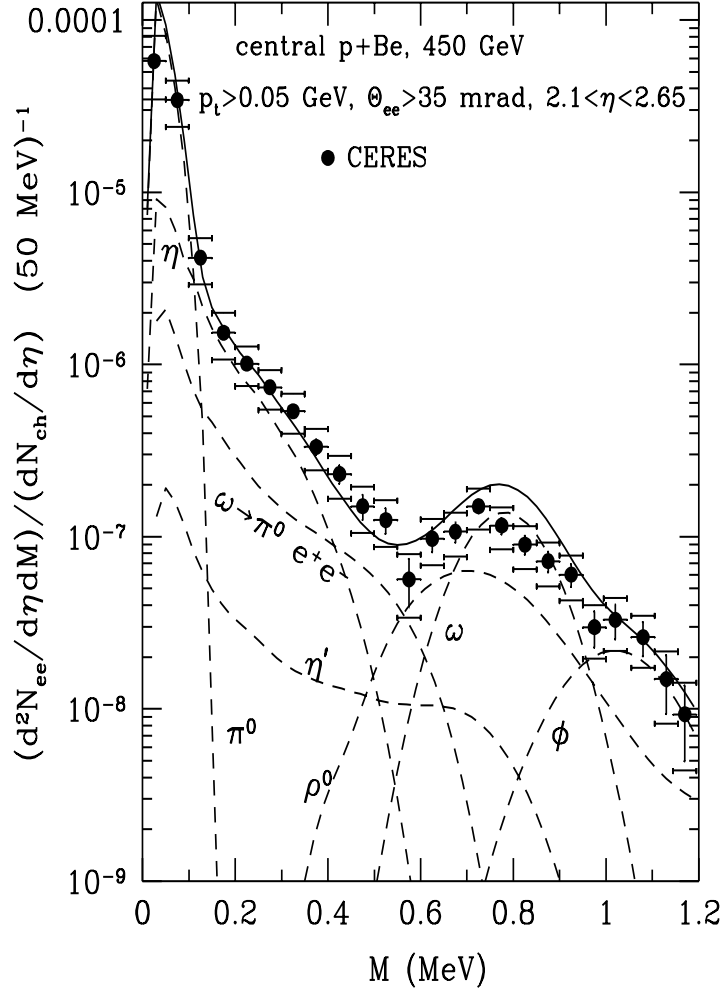


Fig. 1

FIG. 1. Dilepton invariant mass spectra from p+Be collisions at 450 GeV after including the experimental acceptance cuts and mass resolution. Dashed curves give the dilepton spectra from different sources. Experimental data from the CERES collaboration [34] are shown by solid circles, with the statistical errors given by bars. Brackets represent the square root of the quadratic sum of systematic and statistical errors.

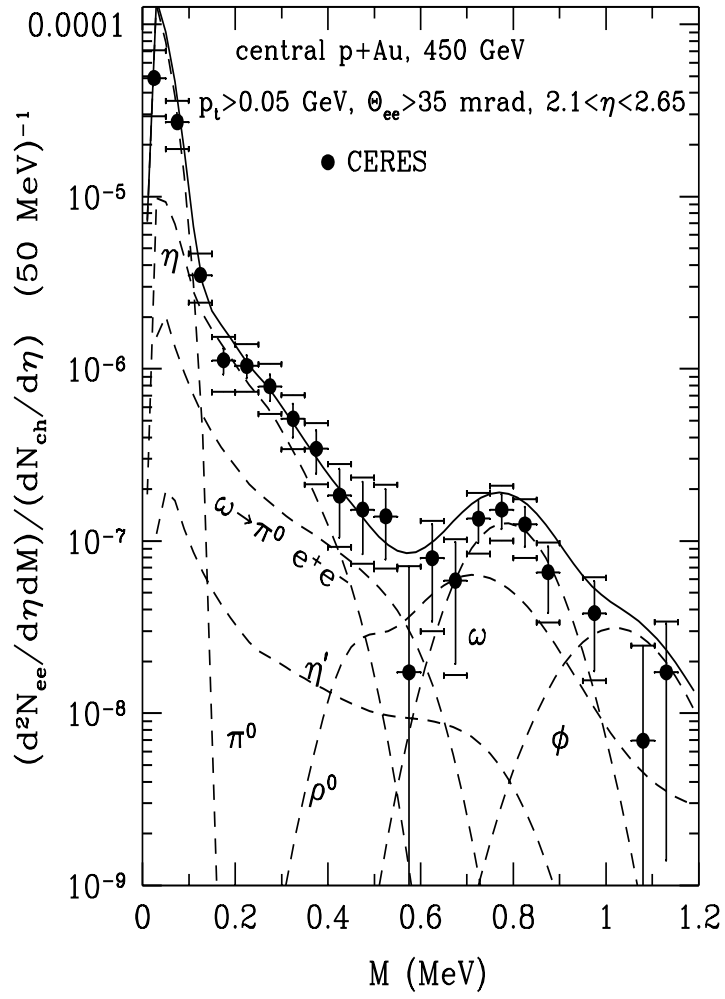


Fig. 2

FIG. 2. Same as Fig. 1 for p+Au collisions.

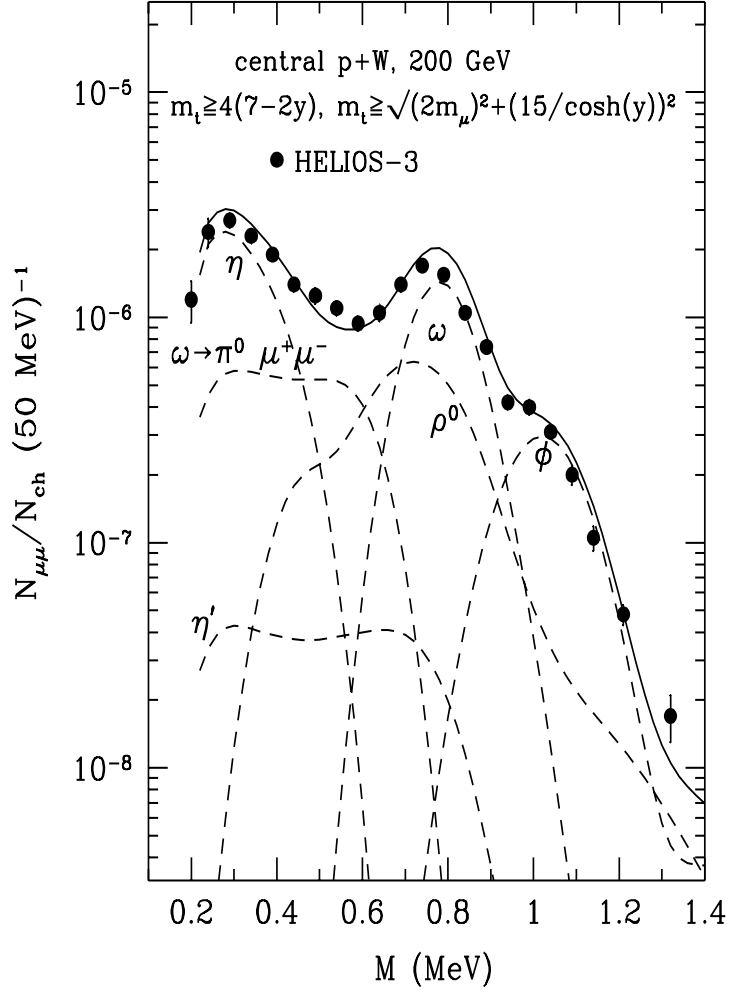


Fig. 3

FIG. 3. Dilepton invariant mass spectra from p+W collisions at 200 GeV after including the experimental acceptance cuts and mass resolution. Dashed curves give the dilepton spectra from different sources. Experimental data from the HELIOS-3 collaboration [35] are shown by solid circles.

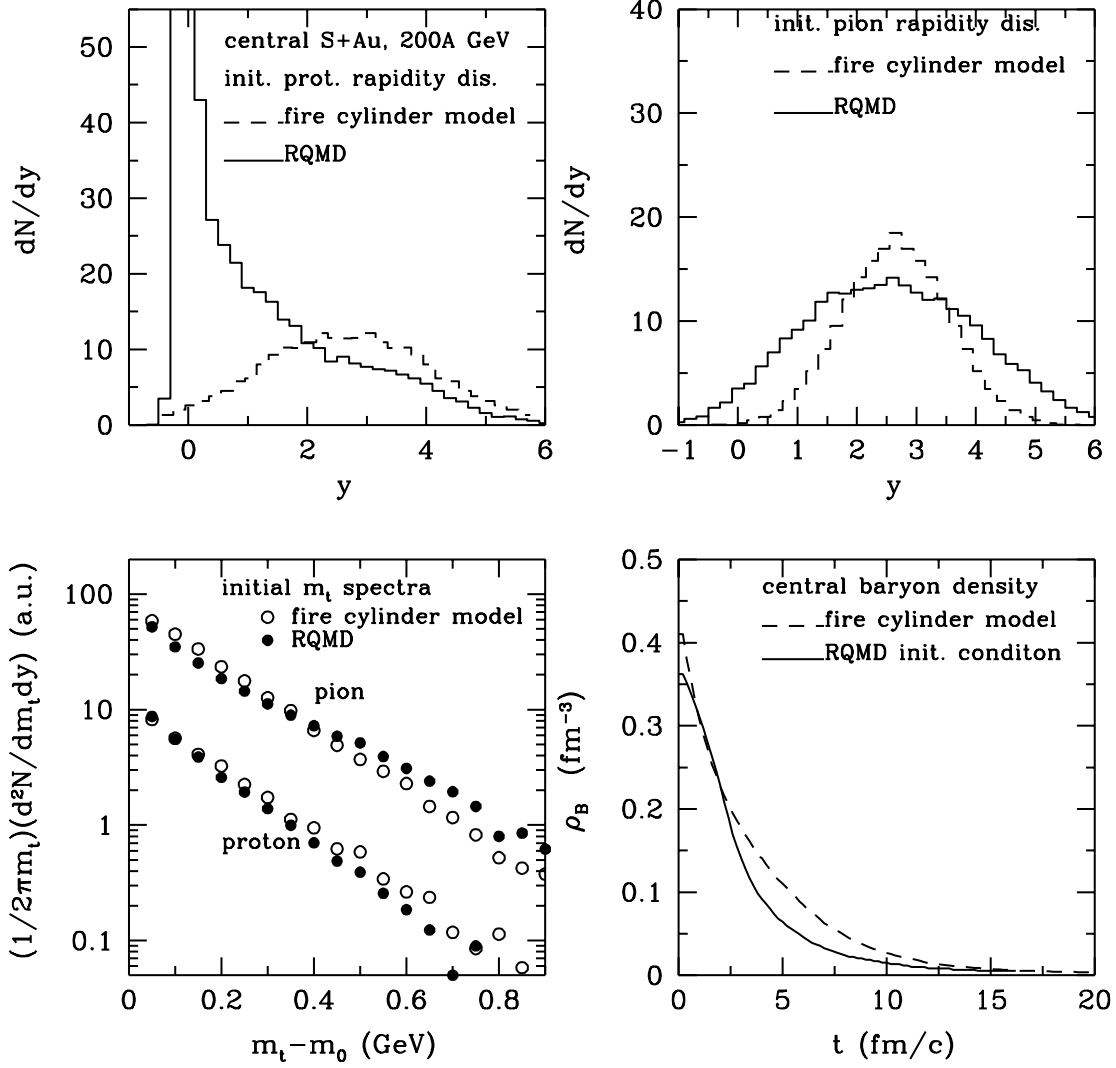


FIG. 4. The initial proton and pion rapidity and transverse mass distributions from both the RQMD and the fire-cylinder model of [36] for S+Au collisions at 200 GeV/nucleon. Also shown is the time evolution of the baryon density using the two initial conditions.

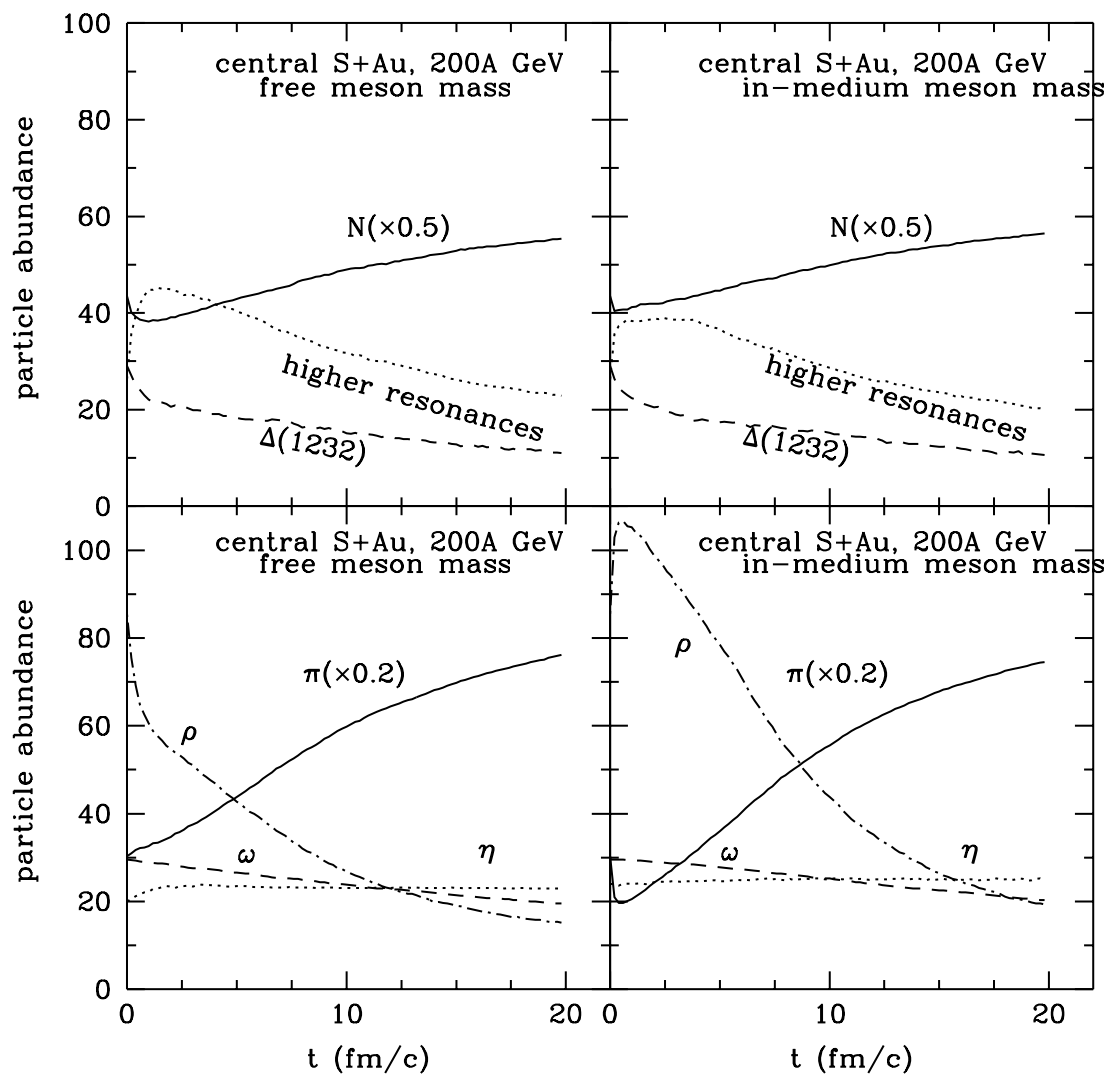


FIG. 5. The time evolution of hadron abundance in central S+Au collisions at 200 GeV/nucleon.

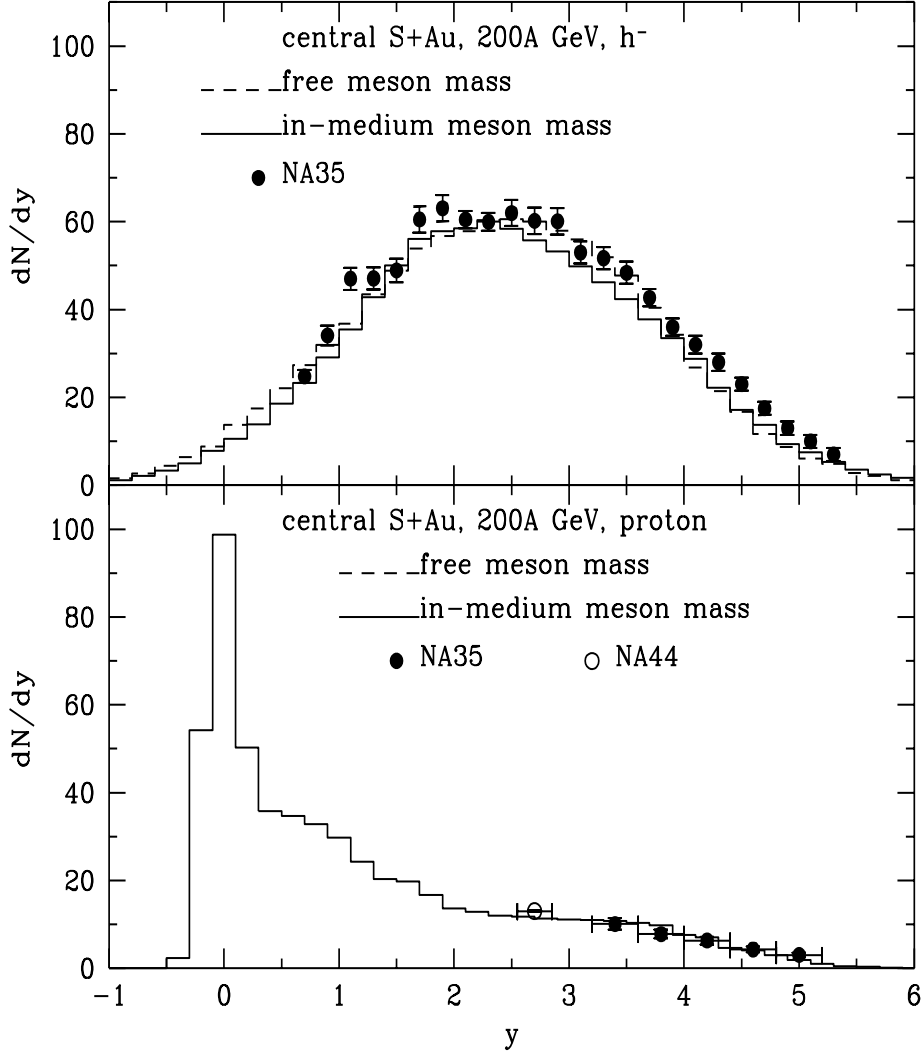


FIG. 6. The rapidity distributions of negatively-charged hadrons and protons. Experimental data from the NA35 collaboration [61] are shown by solid circles, and that from NA44 [62] are shown by open circle.

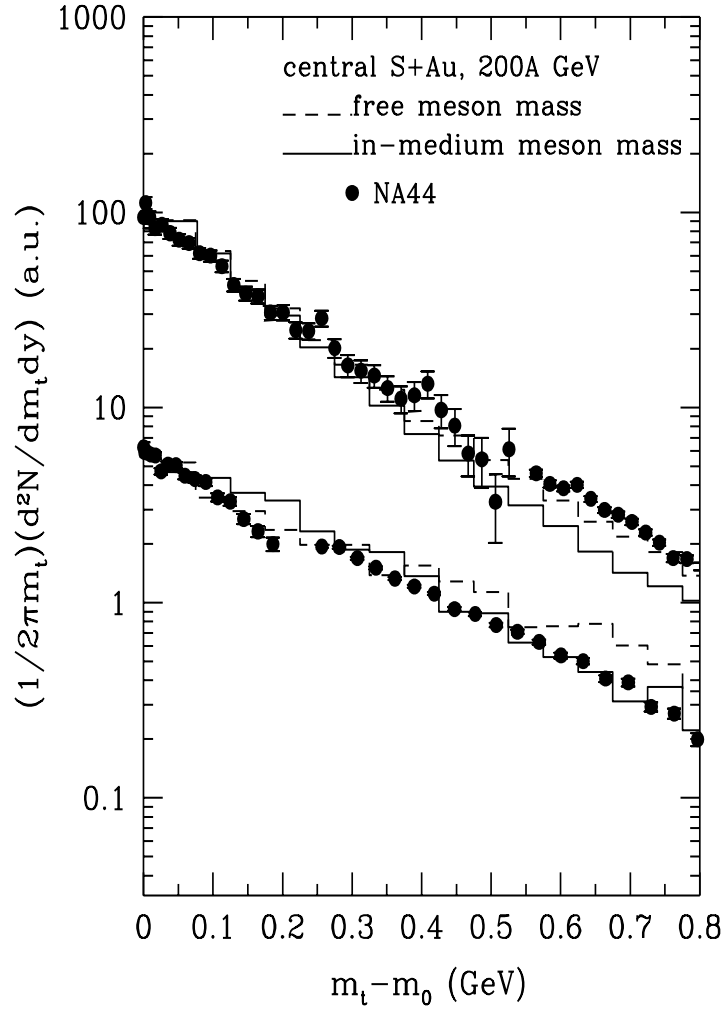


FIG. 7. The transverse mass spectra of protons and pions in the mid- to forward-rapidity region. Experimental data from central S+Pb collisions by the NA44 collaboration [62] are shown by solid circles.

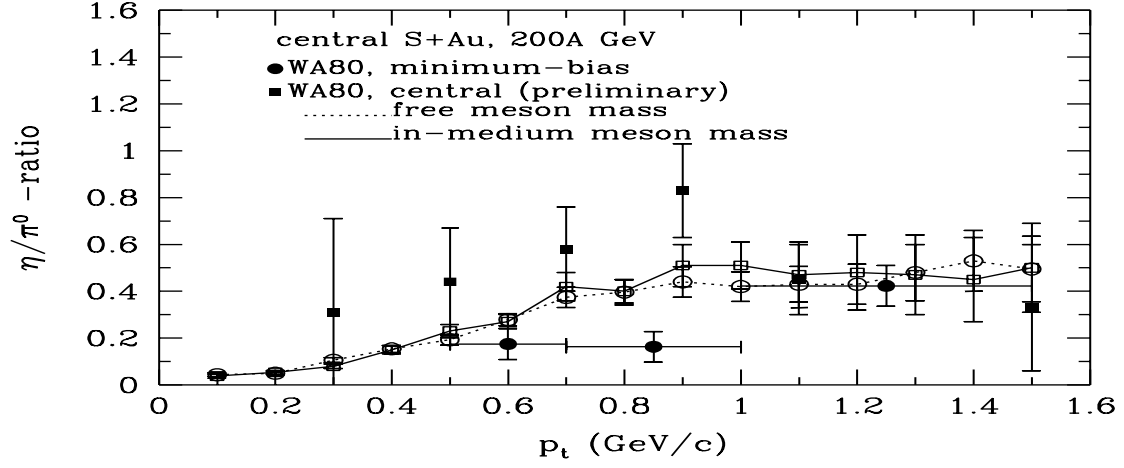


FIG. 8. The  $\eta/\pi^0$  ratio as a function of transverse momentum. Open circles and squares are theoretical results with free and in-medium meson masses, respectively. Solid circles and squares are the WA80 data for minimum-biased and central collisions, respectively.

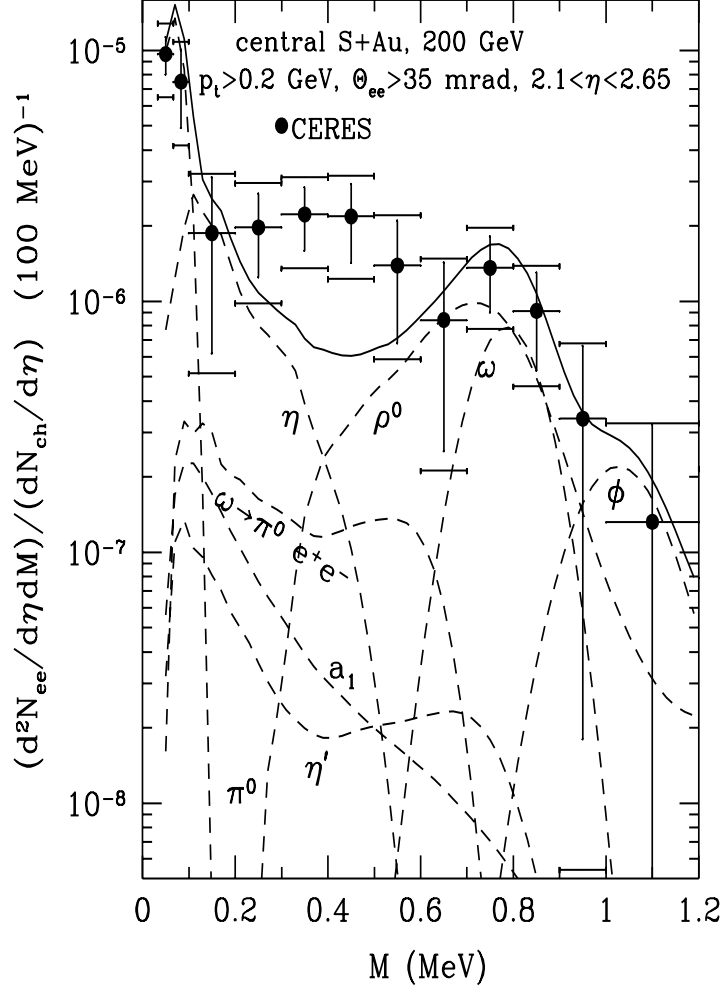


FIG. 9. Dilepton invariant mass spectra from S+Au collisions at 200 GeV using free meson masses and after including the experimental acceptance cuts and mass resolution. Dashed curves give the dilepton spectra from different sources. Experimental data from the CERES collaboration [34] are shown by solid circles, with the statistical errors given by bars. Brackets represent the square root of the quadratic sum of systematic and statistical errors.

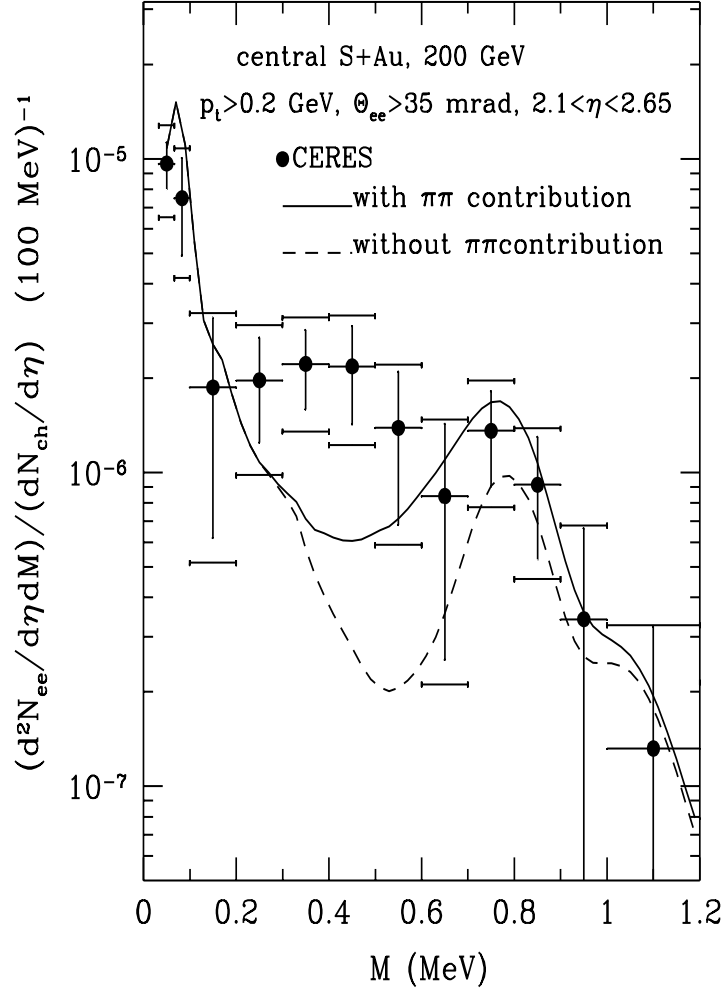


FIG. 10. The importance of pion-pion annihilation contribution to dilepton spectra.

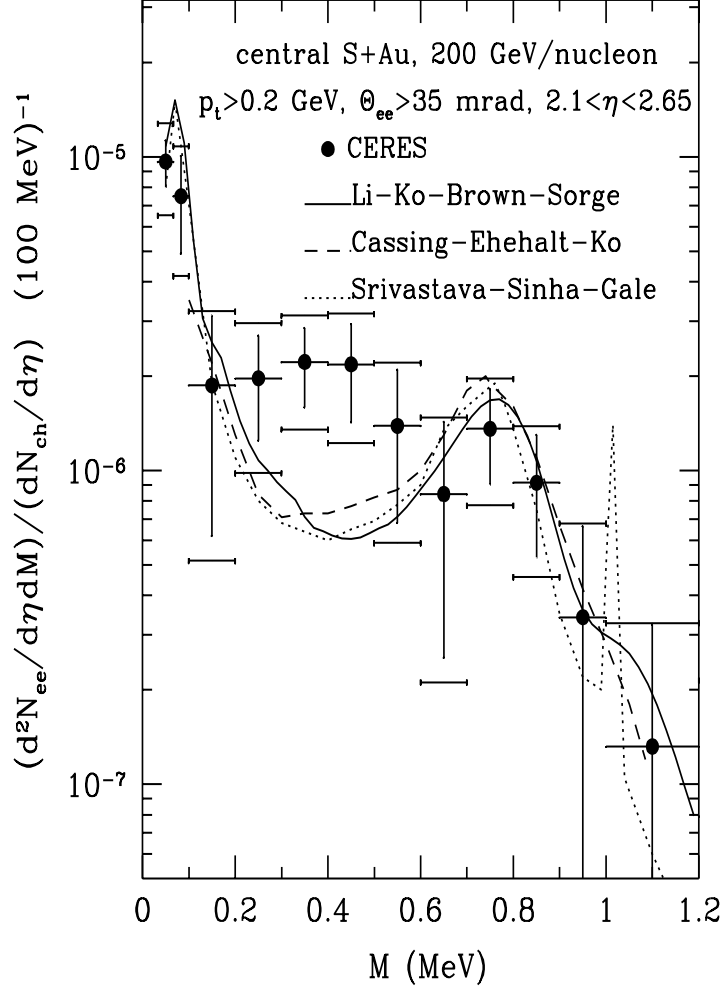


FIG. 11. Comparisons of dilepton spectra in central S+Au collisions from three different model calculations. The solid curve is from this work, the dashed curve is from Ref. [37], and the dotted curve is from Ref. [39].

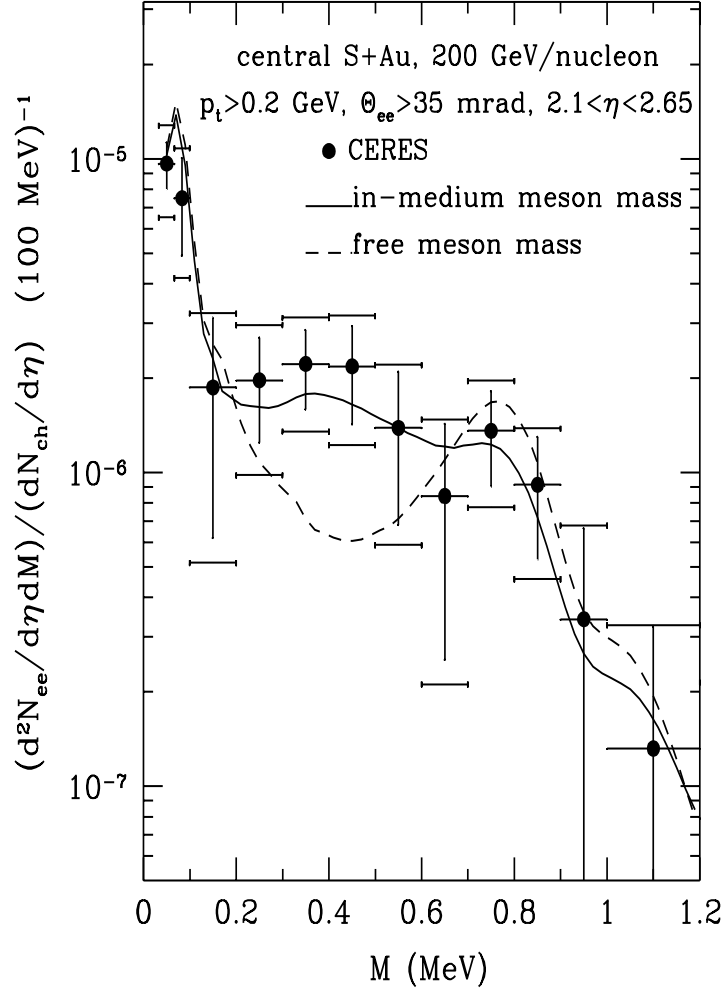


FIG. 12. Dilepton invariant mass spectra from central S+Au collisions with free (dashed curve) and in-medium (solid curve) meson masses.

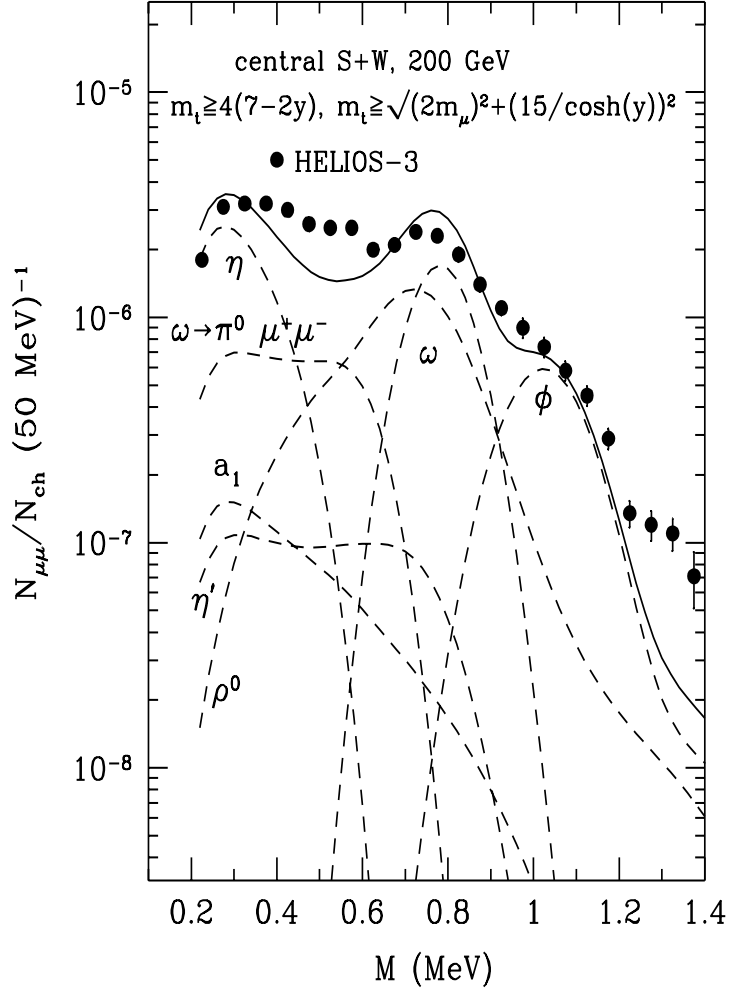


FIG. 13. Dilepton invariant mass spectra from S+W collisions at 200 GeV using free meson masses and after the including experimental acceptance cuts and mass resolution. Dashed curves give the contributions from different sources. Experimental data from the HELIOS-3 collaboration [35] are shown by solid circles.

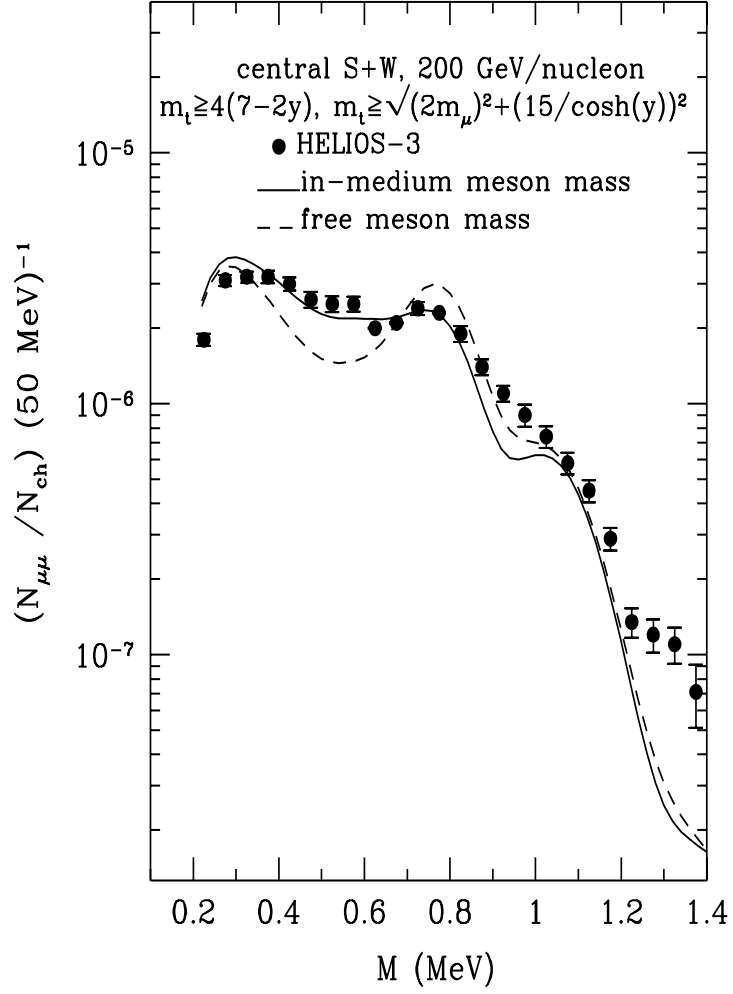


FIG. 14. Dilepton invariant mass spectra from S+W collisions at 200 GeV with free (dashed curve) and in-medium (solid curve) meson masses.

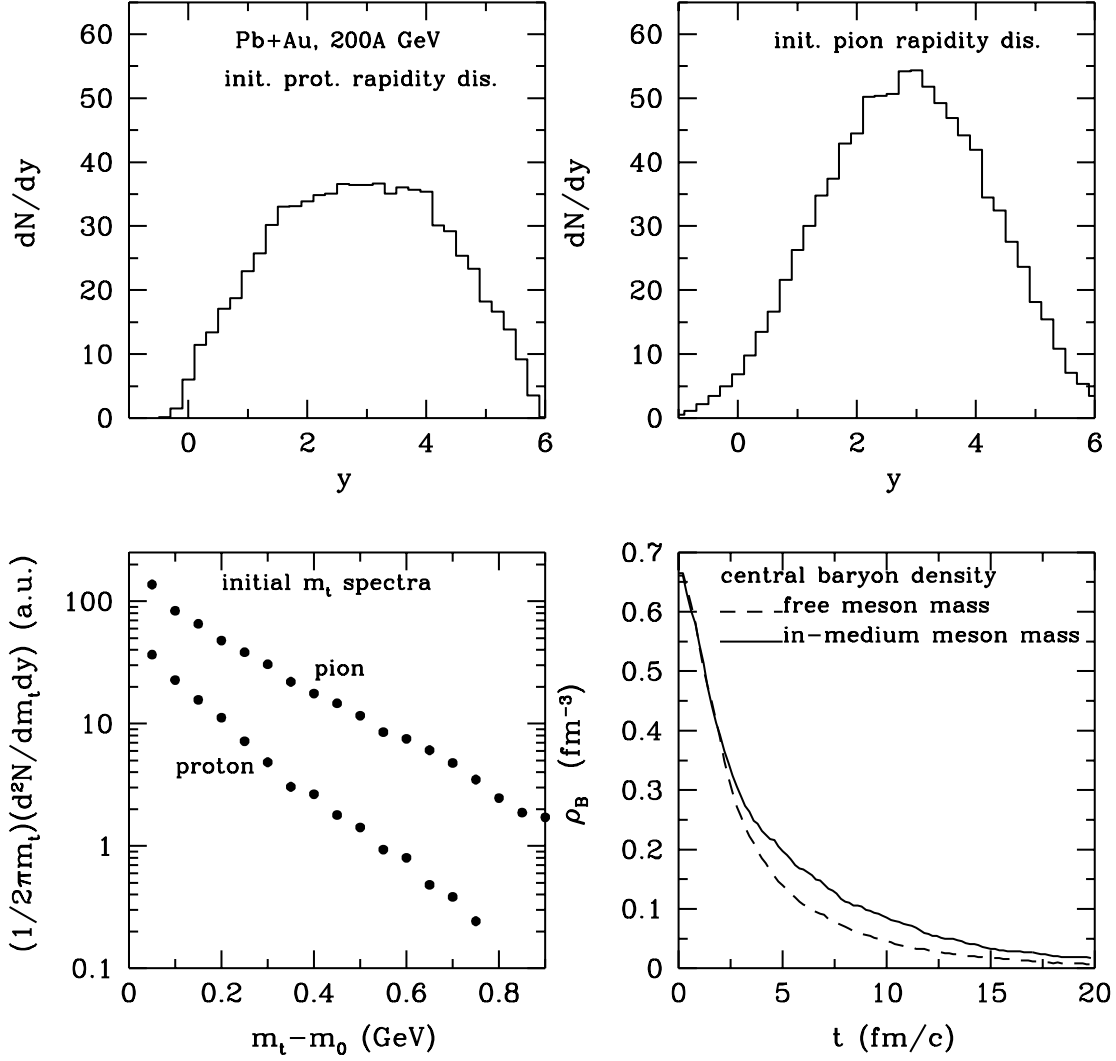


FIG. 15. The initial proton and pion rapidity and transverse mass distributions in central Pb+Au collisions at 160 GeV/nucleon. Also shown is the time evolution of the baryon density.

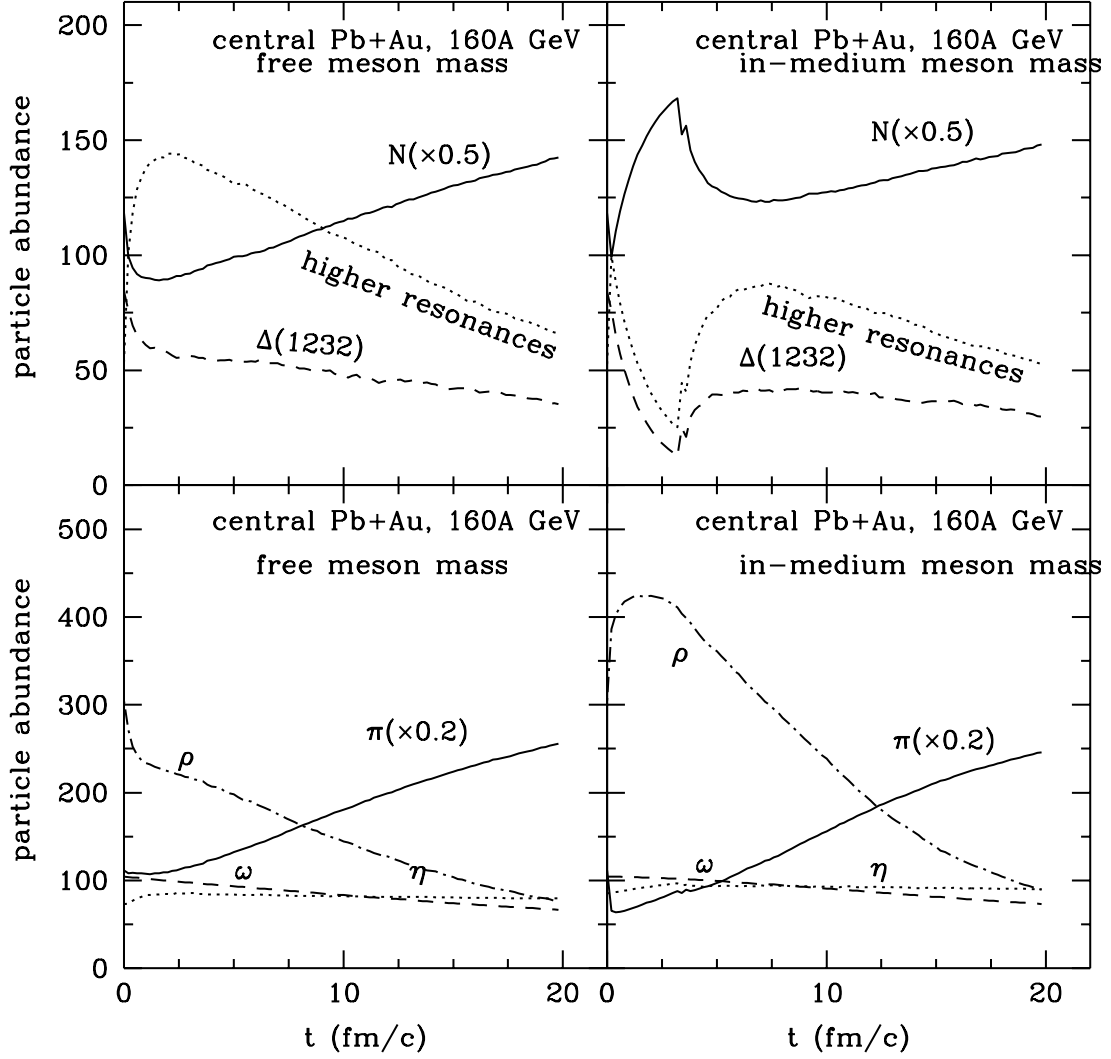


FIG. 16. The time evolution of hadron abundance in central Pb+Au collisions at 160 GeV/nucleon.

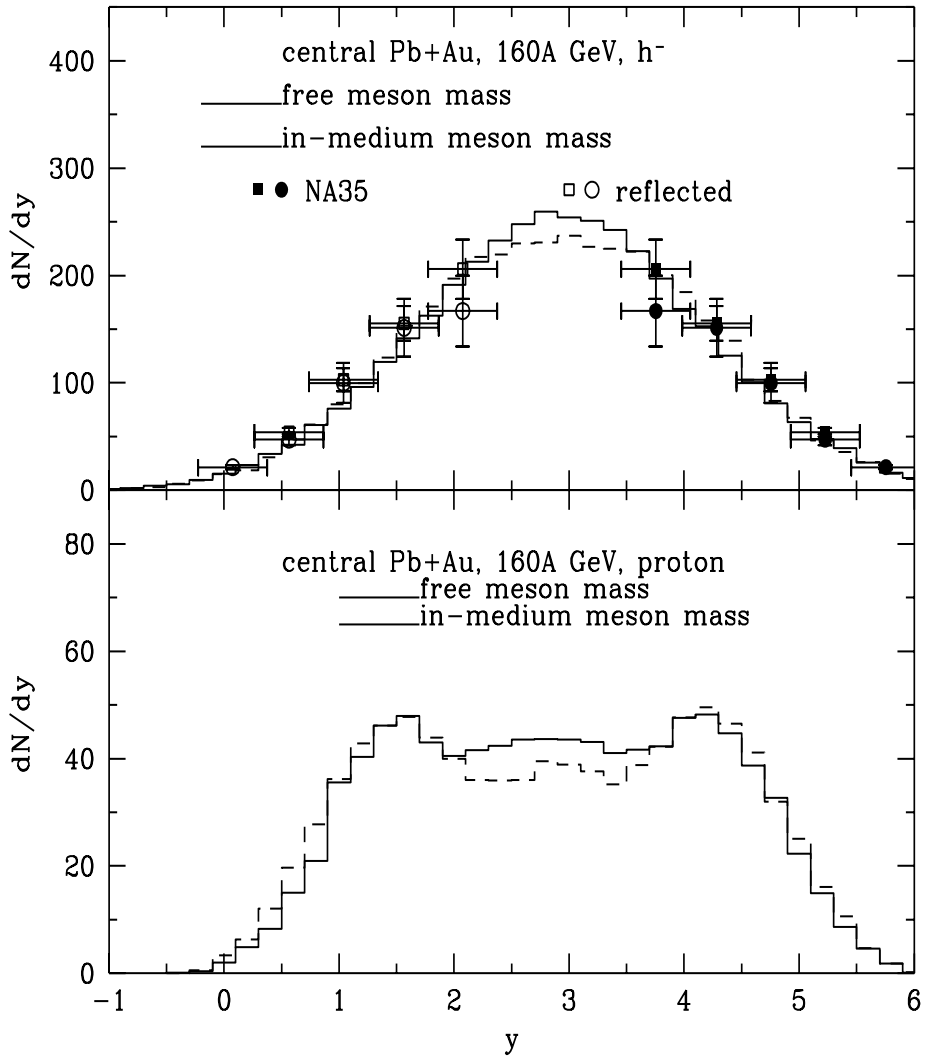


FIG. 17. The rapidity distributions of negatively-charged hadrons and protons in central Pb+Au collisions at 160 GeV/nucleon. Experimental data from the NA49 collaboration [61] are shown by circles.

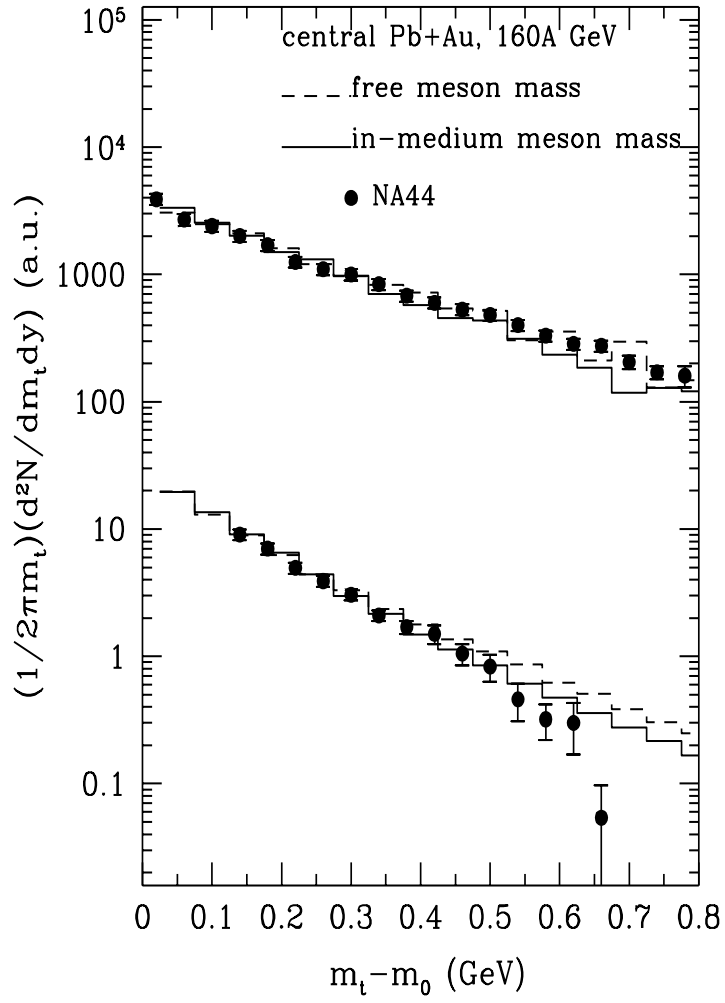


FIG. 18. The transverse mass spectra of protons and pions in the mid- to forward-rapidity region from central Pb+Au collisions at 160 GeV/nucleon. Experimental data from the NA44 collaboration [62] are shown by solid circles.

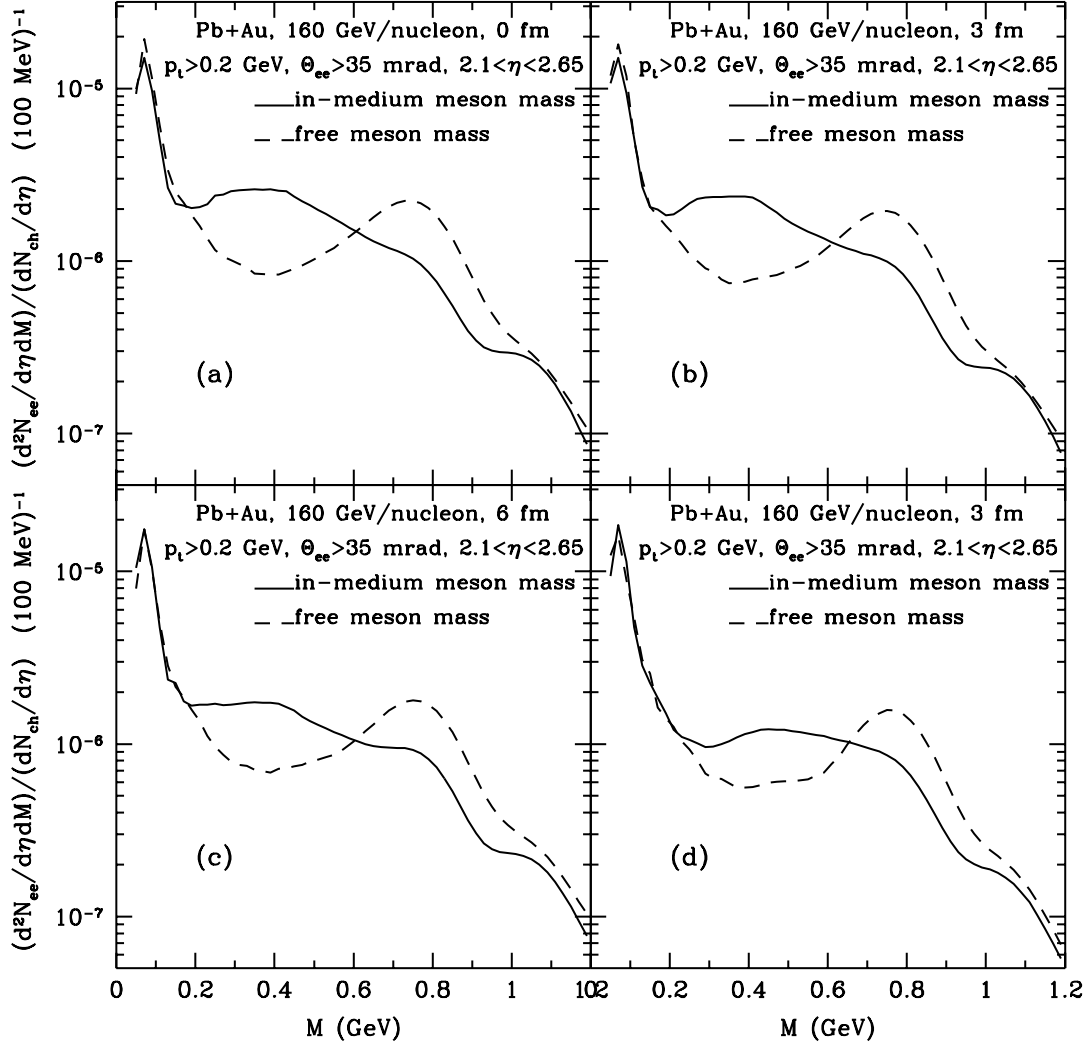


FIG. 19. Dilepton spectra from Pb+Au collisions with free (dashed curves) and in-medium (solid curves) meson masses for the impact parameters (a) 0, (b) 3, (c) 6, and (d) 9 fm. The CERES mass resolution and acceptance cuts for the S+Au collisions are included.

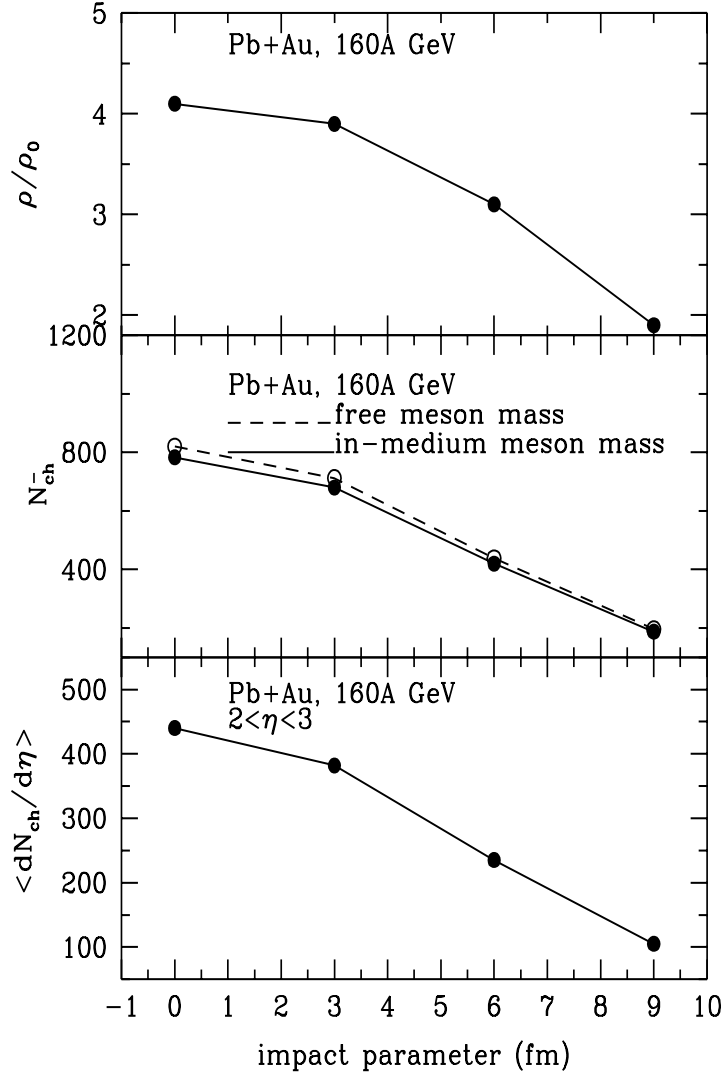


FIG. 20. Impact parameter dependence of the initial average baryon density, the final negatively-charged particle multiplicity, and the charge particle pseudorapidity density at midrapidity for Pb+Au collisions at 160 GeV/nucleon.

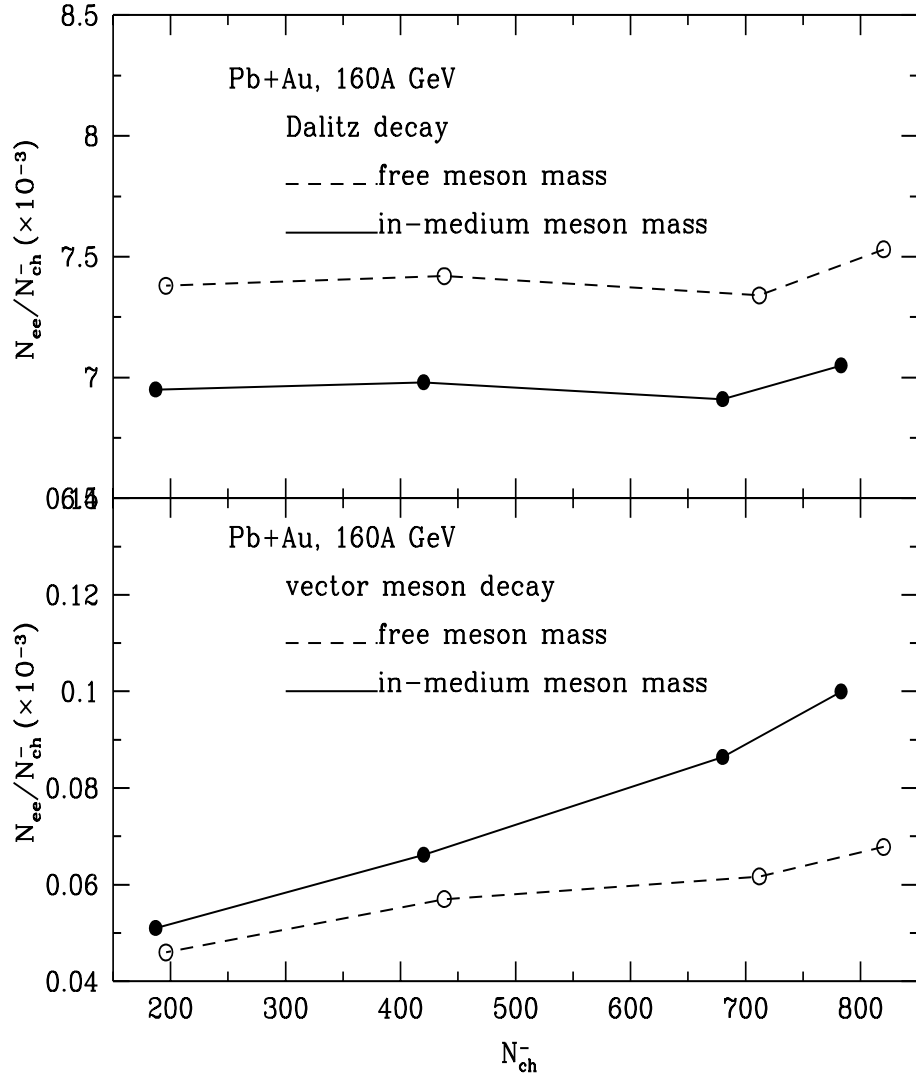


FIG. 21. The normalized total dilepton yield as a function of the total negatively-charged hadron multiplicity in Pb+Au collisions at 160 GeV/nucleon.